

An Improved PWM Strategy for Z-source Inverter with Maximum Boost Capability and Minimum Switching Frequency

Yan Zhang, *Member, IEEE*, Jinjun Liu, *Senior Member, IEEE*, Xinying Li, *Student Member, IEEE*
Xiaolong Ma, Sizhan Zhou, Hongliang Wang, *Senior Member, IEEE*, Yanfei Liu, *Fellow, IEEE*

Abstract—Z-source inverter provides a competitive single-stage DC-AC power conversion with the capability of both buck and boost voltage regulation. In order to maximize voltage gain and to increase efficiency, this paper proposes an improved pulse-width modulation (PWM) strategy. By adjusting the shoot-through (ST) duty ratio of one-phase leg, it regulates the average value of intermediate dc-link voltage which is the same as the instantaneous maximum of three-phase line voltage in one switching time period (T_s). And the other two-phase legs maintain the fixed switching states. Thus, the equivalent switching frequency of power devices in the inverter bridge is reduced to $1/3f_s$ (f_s is the frequency corresponding to T_s). The operating principles and closed-loop controller design are analyzed and verified by simulation and experiments. Compared with existing PWM strategies, the improved PWM strategy demonstrates higher efficiency under full operation range of low voltage gain (1.27~2) application. However, with the improved PWM strategy, the inductor current and capacitor voltage contain six-time-line-frequency ripples, which consequently require large size of the passive components when the output frequency is very low. Thus, it is also suitable for 400-800Hz medium frequency aircraft and vessel power supply system due to a relatively high output line frequency. Furthermore, the idea of improved PWM strategy can be extended to other kinds of three-phase impedance network based inverters.

Index Terms— Closed-loop Control, DC/AC Conversion, Minimum Switching Frequency, Pulse-width Modulation (PWM) Strategy, Voltage Gain, Z-source Inverter.

I. INTRODUCTION

CONVENTIONAL two-level three-phase voltage source inverter (VSI) can only perform buck voltage regulation. For applications requiring both buck and boost power conversion, an additional boost DC-DC converter is required in the front. In view of two-stage power conversion increasing

system cost and lowering efficiency, Peng [3] proposed Z-source inverter, shown in Fig.1, introducing a unique impedance network between the source and the inverter bridge. It achieves voltage boost capability by advantageously adopting shoot-through (ST) of inverter-bridge legs, which provides a potential low-cost, high-efficiency and single-stage power conversion when the boost ratio is low (1-2) [33]. Furthermore, the shoot-through (ST) permission of inverter- bridge legs and elimination of dead-zone time are beneficial to improve the system reliability and quality of output waveforms. Since Z-source inverter overcomes the limitations of traditional VSI, various new topologies [4]-[14], pulse-width modulation (PWM) strategies [15]-[26], model and control methods [27]-[31] were proposed to improve its performance.

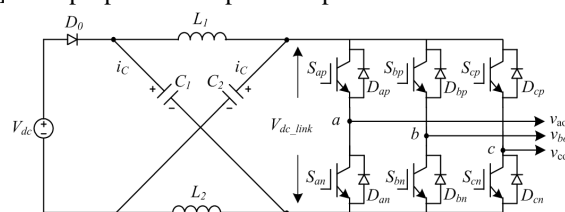


Fig.1 Z-source inverter.

The existing widely used PWM strategies for Z source inverter include simple constant boost control (SCPWM) [3], maximum boost control (MPWM) [16] and maximum constant boost control (MCPWM) [17], according to the intermediate dc-link voltage utilization. SCPWM uses carrier wave based sinusoidal pulse-width modulation (SPWM), and it has the drawback of insufficient dc-link voltage utilization. In order to increase voltage gain as well as to reduce voltage stress of switching devices, Peng [16] proposed MPWM which utilizes all the zero states for ST interval. However, the periodic ST interval causes the six-time-line-frequency (6ω) ripples in the dc-side impedance network. In order to alleviate the undesired influence of low frequency ripples, Shen [17] proposed MCPWM with fixed ST interval. According to the distribution of ST current in three-phase legs, there are two major categories: single-phase leg ST (1P ST) and three-phase leg ST (3P ST) [19] [20]. 1P ST method inserts ST interval by overlapping the upper and lower switches in each phase leg at every switching commutation. Thus, the ST interval is averagely divided into six parts in one switching time period (T_s), which is beneficial to

Manuscript received May 27, 2016; revised Dec 14, 2016; accepted Jan 22, 2017. This work was supported in part by the State Key Laboratory of Electrical Insulation and Power Equipment under the Grant EIPE14112 and EIPE16310 and the Power Electronics Science and Education Development Program of Delta Environmental & Educational Foundation under Grant DREG2016010.

Yan Zhang, Jinjun Liu, Xinying Li, Xiaolong Ma, Sizhan Zhou are with the State Key Lab of Electrical Insulation and Power Equipment, School of Electrical Engineering, Xi'an Jiaotong University, Xi'an 710049, China. (E-mail: zhangyanjtu@mail.xjtu.edu.cn; jjliu@mail.xjtu.edu.cn).

Hongliang Wang, and Yanfei Liu are with the Department of Electrical and Computer Engineering, Queen's University, Kingston, ON K7L 3N6 Canada.

reduce the volume of inductors considerably. 3P ST method inserts ST interval in three-phase legs simultaneously. The instantaneous ST current is averagely distributed among three-phase legs, which is beneficial to reduce the current stress and conduction loss of power devices. However, it introduces an additional switching commutation.

This paper starts by reviewing typical PWM strategies of Z-source inverter through modification of the conventional VSI PWM strategies (e.g. SPWM and SVM) in Section II, and then proposes an improved PWM strategy with maximum voltage gain and minimum switching frequency in Section III. By adjusting the ST duty ratio of one phase leg, it regulates the average value of intermediate dc-link voltage which is the same as the instantaneous maximum of three-phase line voltage in one switching time period (T_s). As a result, the equivalent switching frequency of power devices in the inverter bridge is reduced to $1/3f_s$ ($f_s=1/T_s$), which makes a great contribution to the reduction of switching losses. After that, a comprehensive comparison between the improved PWM strategy and existing PWM strategies is carried out in terms of power device and passive component requirements in Section IV. The detailed closed-loop controller design is investigated in Section V. Simulation and experiment verification are presented in Section VI. The conclusion of this study is outlined in the last Section.

II. TYPICAL PWM STRATEGIES OF Z-SOURCE INVERTER

The aforementioned PWM strategies including simple constant boost control (SCPWM), maximum boost control (MPWM) and maximum constant boost control (MCPWM) can use either single-phase leg ST (1P ST) or three-phase legs ST (3P ST). They are referred as SCPWM+1P ST, SCPWM+ 3P ST, MCPWM+1P ST, MCPWM+3P ST, MPWM+1P ST, MPWM+3P ST in this study. Usually, all these six typical PWM strategies can be derived by modifying the modulation waveforms of conventional three-phase VSI.

Figs.2 and 3 show the main circuit of conventional three-phase VSI and three typical PWM strategies including SPWM, SPWM with 3th harmonic injection (SPWM+3th) or space vector modulation (SVM). Three-phase symmetrical output voltage and output power can be expressed as below:

$$\begin{cases} v_{ao}(\omega t) = \hat{v}_{ac} \cdot \cos(\omega t) \\ v_{bo}(\omega t) = \hat{v}_{ac} \cdot \cos(\omega t - \frac{2}{3}\pi) \\ v_{co}(\omega t) = \hat{v}_{ac} \cdot \cos(\omega t + \frac{2}{3}\pi) \end{cases} \quad (1)$$

$$P_o = \frac{3}{2} \cdot \hat{v}_{ac} \cdot \hat{i}_{ac} \cos(\varphi) \quad (2)$$

Where: \hat{v}_{ac} and \hat{i}_{ac} are the peak value of phase voltage and current. $\cos(\varphi)$ is the load power factor. $\omega = 2\pi f_{line}$, f_{line} is the fundamental frequency of output phase voltage.

The voltage gain, as well as modulation index, is defined as \hat{v}_{ac} over half of dc-link voltage.

$$M_i = \frac{\hat{v}_{ac}}{v_{dc}/2} \quad (3)$$

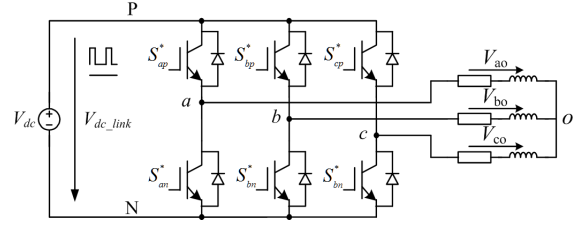


Fig.2 Three-phase VSI.

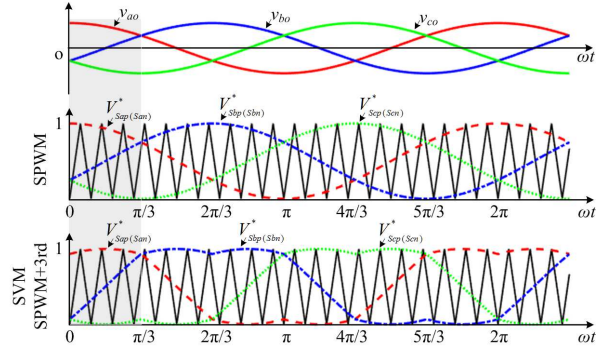


Fig.3 The equivalent modulation waveforms of carrier wave based SPWM and SVM.

As is shown in Fig.3, based on the assumption that the amplitude of triangular waveform is normalized, the expressions of three-phase modulation waveforms for SPWM and SVM (in the first sextant) are expressed as (4) and (5), respectively. Compared with SPWM, SVM can increase the maximum voltage gain to $2/\sqrt{3}$.

$$\begin{cases} V_{Sap(San)}^*(\omega t) = \frac{1}{2} + \frac{M_i}{2} \cdot \cos(\omega t) \\ V_{Sbp(Sbn)}^*(\omega t) = \frac{1}{2} + \frac{M_i}{2} \cdot \cos(\omega t - \frac{2}{3}\pi) \\ V_{Scp(Scn)}^*(\omega t) = \frac{1}{2} + \frac{M_i}{2} \cdot \cos(\omega t + \frac{2}{3}\pi) \end{cases} \quad \text{For SPWM (4)}$$

Where: $0 \leq M_i \leq 1$, $0 \leq \omega t \leq 2\pi$.

$$\begin{cases} V_{Sap(San)}^*(\omega t) = \frac{1}{2} + \frac{\sqrt{3}M_i}{4} \cdot \cos(\omega t - \frac{\pi}{6}) \\ V_{Sbp(Sbn)}^*(\omega t) = \frac{1}{2} - \frac{3M_i}{4} \cdot \cos(\omega t + \frac{\pi}{3}) \\ V_{Scp(Scn)}^*(\omega t) = \frac{1}{2} - \frac{\sqrt{3}M_i}{4} \cdot \cos(\omega t - \frac{\pi}{6}) \end{cases} \quad \text{For SVM (5)}$$

Where: $0 \leq M_i \leq \frac{2}{\sqrt{3}}$, $0 \leq \omega t \leq \frac{\pi}{3}$.

Fig.4 shows the switching state of SPWM or SVM in the first sextant. The comparison results of modulation waveforms and triangular wave are adopted to control the switching state of the upper and lower switches in each phase. Thus, the on-state duty ratio of upper and lower switches are $d_{Sip}^*(\omega t) = V_{Sip}^*(\omega t)$, $d_{Sin}^*(\omega t) = 1 - V_{Sip}^*(\omega t)$, (i represents a, b or c).

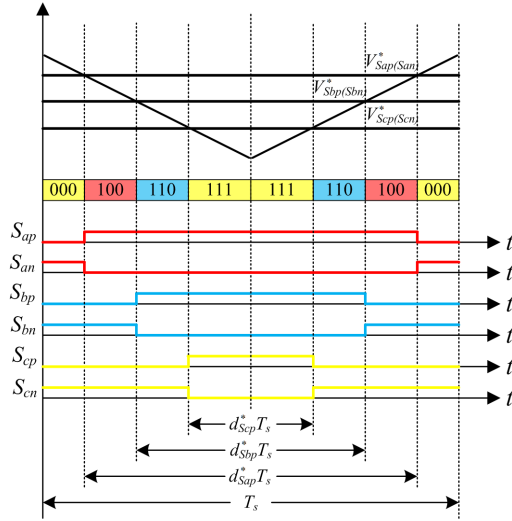


Fig.4 Switching states of SPWM or SVM in the first sextant ($0 \leq \omega t \leq \pi/3$).

As described in Peng [1], voltage gain of Z source inverter is defined as the ratio of the peak phase voltage \hat{v}_{ac} over half of dc source voltage.

$$G = \frac{\hat{v}_{ac}}{V_{dc}/2} = B \cdot M_i \quad (6)$$

In which:
$$B = \frac{1}{1 - 2d_{ST}} \quad (7)$$

Where: M_i is the modulation index, and B is the boost factor determined by d_{ST} .

The obtainable d_{ST} increases with the decrease of M_i . As described in Shen [17], d_{ST} and M_i meet:

$$d_{ST} = 1 - M_i \quad (0 \leq M_i \leq 1) \quad \text{for SCPWM} \quad (8)$$

$$d_{ST} = 1 - \frac{\sqrt{3}}{2} M_i \quad (0 \leq M_i \leq \frac{2}{\sqrt{3}}) \quad \text{for MCPWM} \quad (9)$$

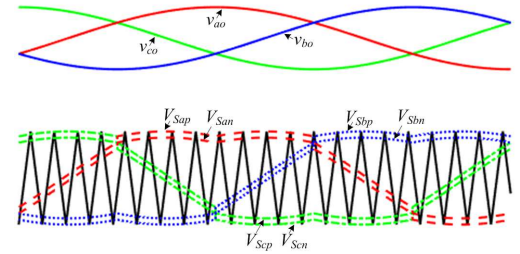
$$d_{ST}(\omega t) = 1 - \frac{\sqrt{3}}{2} M_i \cos(\omega t - \frac{\pi}{6}) \quad (0 \leq \omega t \leq \frac{\pi}{3}, 0 \leq M_i \leq \frac{2}{\sqrt{3}}) \quad \text{for MPWM} \quad (10)$$

A. SCPWM + 1P ST and MCPWM + 1P ST

Fig.5 shows the equivalent carrier wave based PWM and the switching state for MCPWM+1P ST. The ST interval is divided into six parts and averagely inserted in each phase by overlapping the upper and lower switches at every switching commutation. The control reference of six switches for Z-source inverter can be obtained as (11) by shifting the modulation waveforms of conventional three-phase VSI [19]. V_{max}^* , V_{mid}^* , V_{min}^* refer to the modulation waveform of conventional three-phase VSI. Take the first sextant for example, the output voltage meets $v_{ao} > v_{bo} > v_{co}$, So $V_{max}^* = V_{Sap}^*(San)$, $V_{mid}^* = V_{Sbp}^*(Sbn)$, $V_{min}^* = V_{Scp}^*(Scn)$ in (4) or (5). $V_{Sap} = V_{max-Sp}$, $V_{San} = V_{max-Sn}$, $V_{Sbp} = V_{mid-Sp}$, $V_{Sbn} = V_{mid-Sn}$, $V_{Scp} = V_{min-Sp}$, $V_{Scn} = V_{min-Sn}$ are the modified modulation waveform expressions for MCPWM+1P ST in Fig.5.

$$\begin{cases} V_{max-Sp}(\omega t) = V_{max}^*(\omega t) + \frac{1}{2} d_{ST}(\omega t) \\ V_{max-Sn}(\omega t) = V_{max}^*(\omega t) + \frac{1}{6} d_{ST}(\omega t) \\ V_{mid-Sp}(\omega t) = V_{mid}^*(\omega t) + \frac{1}{6} d_{ST}(\omega t) \\ V_{mid-Sn}(\omega t) = V_{mid}^*(\omega t) - \frac{1}{6} d_{ST}(\omega t) \\ V_{min-Sp}(\omega t) = V_{min}^*(\omega t) - \frac{1}{6} d_{ST}(\omega t) \\ V_{min-Sn}(\omega t) = V_{min}^*(\omega t) - \frac{1}{2} d_{ST}(\omega t) \end{cases} \quad (11)$$

Where: the subscript *max*, *mid* and *min* refer to the phase of maximum, middle, minimum output voltage.



(a) The equivalent carrier wave-based PWM.
(b) The switching states in the first sextant ($0 \leq \omega t \leq \pi/3$).

Fig.5 Maximum constant boost control with single-phase leg ST (MCPWM+1P ST).

B. SCPWM + 3P ST and MCPWM + 3P ST

Fig.6 shows the equivalent carrier wave based PWM and the switching state for MCPWM + 3P ST. 3P ST method inserts d_{ST} interval in three-phase legs to replace zero state. The instantaneous d_{ST} current is averagely distributed among three-phase legs, which is beneficial to reduce the current stress and conduction loss of power devices. However, it introduces an additional switching commutation. As shown in Fig.6, two

straight lines V_{ST_up} and V_{ST_low} compared with triangular waveform are adopted to control ST interval [17]. During non- ST interval, control references of six switches for Z-source inverter are the same as modulation waveforms of conventional VSI expressed in (5) in the first sextant.

$$\begin{cases} V_{ST_up}(\omega t) = 1 - \frac{1}{2}d_{ST}(\omega t) \\ V_{max-Sp(Sn)}(\omega t) = V_{max}^*(\omega t) \\ V_{mid-Sp(Sn)}(\omega t) = V_{mid}^*(\omega t) \\ V_{min-Sp(Sn)}(\omega t) = V_{min}^*(\omega t) \\ V_{ST_low}(\omega t) = \frac{1}{2}d_{ST}(\omega t) \end{cases} \quad (12)$$

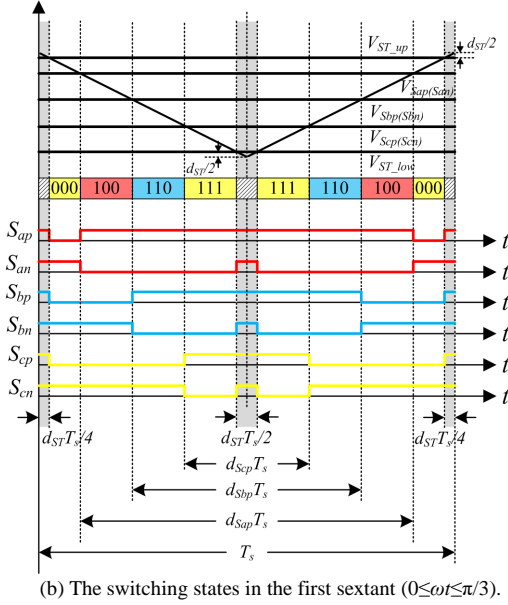
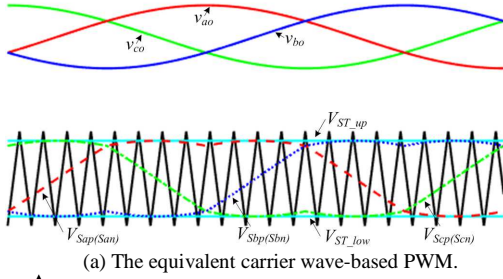
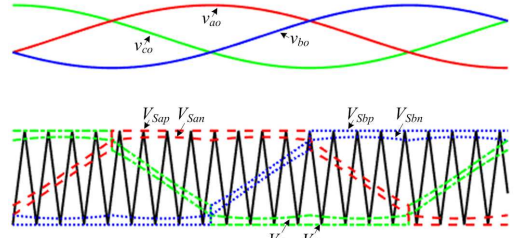


Fig.6 Maximum constant boost control with three-phase legs ST (MCPWM+3P ST).

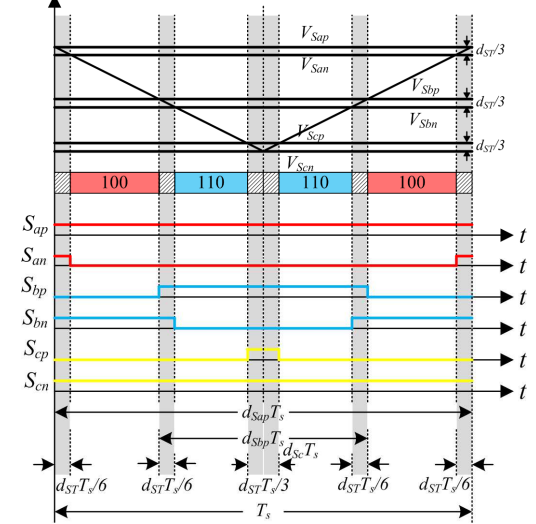
C. MPWM+1P ST

When MPWM is applied, all the zero-state intervals shown in Fig.4 are used for ST. Thus, from (5), the ST duty ratio in the first sextant can be calculated as (10). And it changes with six-time line frequency. Fig.7 shows the equivalent carrier wave-based PWM and the switching state for MPWM+1P ST [16][19]. Substituting (10) into (11), the modulation waveforms of six switches can be rewritten as:

$$\begin{cases} V_{max-Sp}(\omega t) = 1 \\ V_{max-Sn}(\omega t) = V_{max}^*(\omega t) + \frac{1}{6}d_{ST}(\omega t) \\ V_{mid-Sp}(\omega t) = V_{mid}^*(\omega t) + \frac{1}{6}d_{ST}(\omega t) \\ V_{mid-Sn}(\omega t) = V_{mid}^*(\omega t) - \frac{1}{6}d_{ST}(\omega t) \\ V_{min-Sp}(\omega t) = V_{min}^*(\omega t) - \frac{1}{6}d_{ST}(\omega t) \\ V_{min-Sn}(\omega t) = 0 \end{cases} \quad (13)$$



(a) The equivalent carrier wave-based PWM.



(b) The switching states in the first sextant ($0 \leq \omega t \leq \pi/3$).

Fig.7 Maximum boost control with single-phase leg ST (MPWM+1P ST).

D. MPWM + 3P ST

Fig.8 shows the equivalent carrier wave-based PWM and the switching state for MPWM + 3P ST. Two curves V_{ST_up} and V_{ST_low} for ST interval control are the instantaneous maximum and minimum value of three-phase modulation waveforms. The control references of six switches can be written as:

$$\begin{cases} V_{ST_up}(\omega t) = V_{max-Sp(Sn)}(\omega t) \\ V_{max-Sp(Sn)}(\omega t) = V_{max}^*(\omega t) \\ V_{mid-Sp(Sn)}(\omega t) = V_{mid}^*(\omega t) \\ V_{min-Sp(Sn)}(\omega t) = V_{min}^*(\omega t) \\ V_{ST_low}(\omega t) = V_{min-Sp(Sn)}(\omega t) \end{cases} \quad (14)$$

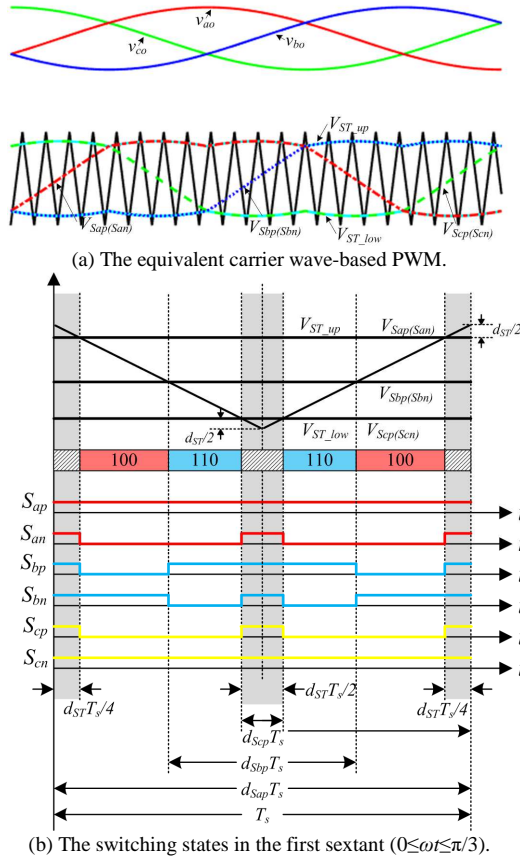


Fig.8 Maximum boost control with three-phase legs ST (MWM+3P ST).

III. IMPROVED PWM STRATEGY OF Z-SOURCE INVERTER

Fig.9 shows the relationship of three-phase output voltage and available minimum dc-link voltage for conventional three-phase VSI with two typical PWM strategies: SPWM and SVM. The fundamental frequency f_{line} is 50Hz for analysis. Using SPWM, the minimum constant dc-link voltage is twice the peak value of output phase voltage $2\hat{v}_{ac}$, which is represented by the green solid line. Using SPWM with 3th harmonic injection or SVM to increase dc-link voltage utilization, the minimum constant dc-link voltage is $\sqrt{3}\hat{v}_{ac}$, which is represented by the blue dot-dash line. Besides, there is another available dc-link voltage which is represented by the magenta dashed line changing with six-time line frequency. It is actually the instantaneous maximum value of three-phase line voltage and it can be expressed as:

$$v_{dc_link}^*(\omega t) = \sqrt{3} \cdot \hat{v}_{ac} \cdot \cos(\theta - \frac{\pi}{6}) \quad (15)$$

Where: θ is the remainder of ωt divided by $\pi/3$, $\theta = \omega t \% (\pi/3)$.

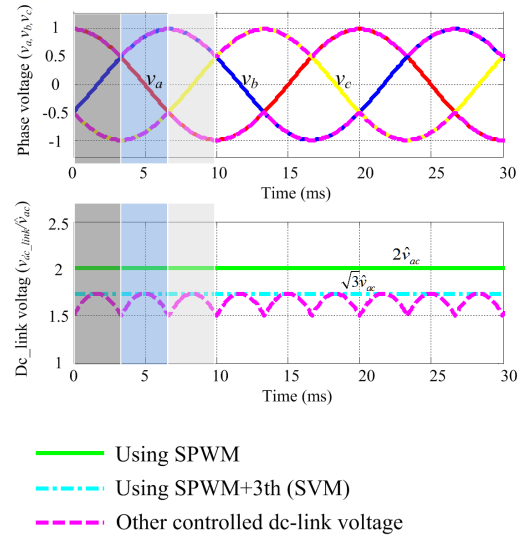


Fig.9 The available dc-link voltage of the inverter bridge.

If the average dc-link voltage in one switching time period $\langle v_{dc_link} \rangle_{T_s}$ can be accurately controlled as the magenta dashed line shown in Fig.9, the upper switch in the leg of the maximum phase voltage (v_{max}) and the lower switch in the leg of minimum phase voltage (v_{min}) are always turned on. The upper and lower switches in the rest phase leg (v_{mid}) are controlled with PWM signal. The switching states of power devices in three-phase legs are listed in Tab.I. The equivalent switching frequency of power devices can be reduced to $1/3f_s$ ($f_s = 1/T_s$). Take the first sextant for example, the instantaneous dc-link voltage is the line voltage ($v_{ao} - v_{co}$). S_{ap} and S_{cn} are always turned on. S_{bp} and S_{bn} are controlled with PWM to regulate v_{bo} . In each sextant, only one phase leg operates under complementary PWM mode. And the corresponding duty ratio of upper and lower switch d_{Sip}^* , d_{Sin}^* are expressed as

$$\begin{cases} d_{Sip}^*(\omega t) = \frac{v_{mid}(\omega t) - v_{min}(\omega t)}{v_{max}(\omega t) - v_{min}(\omega t)} \\ d_{Sin}^*(\omega t) = 1 - d_{Sip}^*(\omega t) \end{cases} \quad (16)$$

Where: in each sextant, $v_{min}(\omega t) = \min(v_{ao}, v_{bo}, v_{co})$; $v_{max}(\omega t) = \max(v_{ao}, v_{bo}, v_{co})$; $v_{mid}(\omega t) = \text{mid}(v_{ao}, v_{bo}, v_{co})$; i representing the phase of $v_{mid}(\omega t)$, changes between a , b , and c .

As for conventional two-stage buck-boost VSI, at the intermediate dc-link, there is a large aluminium electrolytic capacitor to absorb the high frequency current harmonics and compensate the transient power difference between the front boost circuit and inverter bridge [32]. Usually, the intermediate dc-link voltage is kept almost constant by adjusting the boost duty ratio in steady state. It is difficult or even impossible to

TABLE I THE SWITCHING STATES OF POWER DEVICES IN THE INVERTER BRIDGE

Phase angle	$0^\circ \leq \theta \leq 60^\circ$	$60^\circ \leq \theta \leq 120^\circ$	$120^\circ \leq \theta \leq 180^\circ$	$180^\circ \leq \theta \leq 240^\circ$	$240^\circ \leq \theta \leq 300^\circ$	$300^\circ \leq \theta \leq 360^\circ$
Mod A	$S_{ap}=1; S_{an}=0$	$S_{ap} S_{an}=\text{PWM}$	$S_{ap}=0; S_{an}=1$	$S_{ap}=0; S_{an}=1$	$S_{ap} S_{an}=\text{PWM}$	$S_{ap}=1; S_{an}=0$
Mod B	$S_{bp} S_{bn}=\text{PWM}$	$S_{bp}=1; S_{bn}=0$	$S_{bp}=1; S_{bn}=0$	$S_{bp} S_{bn}=\text{PWM}$	$S_{bp}=0; S_{bn}=1$	$S_{bp}=0; S_{bn}=1$
Mod C	$S_{cp}=0; S_{cn}=1$	$S_{cp}=0; S_{cn}=1$	$S_{cp} S_{cn}=\text{PWM}$	$S_{cp}=1; S_{cn}=0$	$S_{cp}=1; S_{cn}=0$	$S_{cp} S_{cn}=\text{PWM}$

control the intermediate dc-link voltage like a six-pulse waveform. However, for Z-source inverter, v_{dc_link} is chopped dc voltage with high switching frequency. Therefore, maybe there is a new PWM strategy that is suitable for Z-source inverter.

According to the operation principles of Z-source inverter described in Peng [3], Fig.10 shows two equivalent circuits seen from the dc-link of the inverter bridge. During ST interval, D_0 is reverse biased and Z-source network is shorted $v_{dc_link} = 0$. During non- ST interval, D_0 is conducting, both capacitors and dc source are reversely connected to supply the inverter bridge $v_{dc_link} = 2V_C - V_{dc}$. Thus, the average intermediate dc-link voltage in one switching time period is calculated in (17).

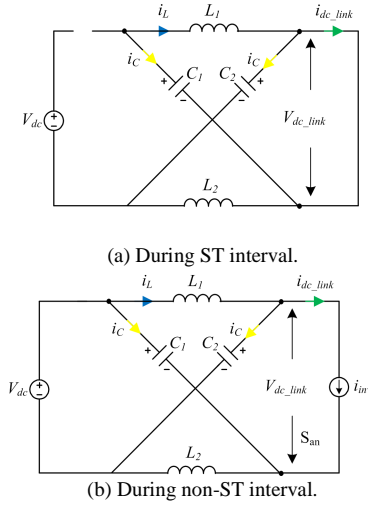


Fig.10 Equivalent circuit of Z source inverter viewed from the dc-link of the inverter bridge.

$$\begin{aligned} \langle v_{dc_link} \rangle_{T_s} &= \frac{1}{T_s} \cdot \left(\int_0^{d_{ST} \cdot T_s} 0 dt + \int_{d_{ST} \cdot T_s}^{T_s} (2V_C - V_{dc}) dt \right) \\ &= (1 - d_{ST}) \cdot (2V_C - V_{dc}) \end{aligned} \quad (17)$$

From (17), $\langle v_{dc_link} \rangle_{T_s}$ can be regulated intermediately by adjusting d_{ST} . For simple analysis, it is assumed that the capacitance of C_1 and C_2 is large enough and the voltage is almost constant in steady state. In order to reduce the switching frequency of power devices in the inverter bridge so that a higher efficiency can be attained, it is possible to regulate $\langle v_{dc_link} \rangle_{T_s}$ to meet (15). Obviously, d_{ST} is periodically changing in every 60 degrees (1/6 output line frequency period).

$$(1 - d_{ST}(\omega t)) \cdot (2V_C - V_{dc}) = \sqrt{3} \cdot \hat{v}_{ac} \cdot \cos(\theta - \frac{\pi}{6}) \quad (18)$$

Where: θ is the remainder of ωt divided by $\pi/3$, $\theta = \omega t \% (\pi/3)$.

In this case, the average voltage of inductor in one sextant should be zero, according to volt-second balance principle.

$$\frac{3}{\pi} \int_0^{\pi/3} (d_{ST}(\omega t) T_s \cdot V_C + (1 - d_{ST}(\omega t)) T_s \cdot (V_{dc} - V_C)) d\omega t = 0 \quad (19)$$

Ignoring the low frequency ripples associated with output line frequency f_s , V_C is determined by the average value of ST duty ratio d_{avg} :

$$V_C = \frac{1 - \frac{3}{\pi} \int_0^{\pi/3} d_{ST}(\omega t) d\omega t}{1 - 2 \cdot \frac{3}{\pi} \int_0^{\pi/3} d_{ST}(\omega t) d\omega t} V_{dc} = \frac{(1 - d_{avg}) V_{dc}}{1 - 2d_{avg}} \quad (20)$$

In which, d_{avg} can be calculated by integrating $d_{ST}(\omega t)$ in (18) in one sextant.

$$\begin{aligned} d_{avg} &= \frac{3}{\pi} \cdot \int_0^{\pi/3} \left(1 - \frac{v_{dc_link}(\omega t)}{2V_C - V_{dc}} \right) \cdot d\omega t \\ &= 1 - \frac{3\sqrt{3}}{\pi} \cdot \frac{\hat{v}_{ac}}{2V_C - V_{dc}} \end{aligned} \quad (21)$$

Solving (6) (20) and (21), the capacitor voltage in steady state can be derived as:

$$V_C = \frac{3\sqrt{3}G}{2\pi} \cdot V_{dc} \quad (22)$$

And the ST duty ratio is

$$d_{ST}(\omega t) = 1 - \frac{\pi}{3} (1 - d_{avg}) \cos(\omega t - \frac{\pi}{6}) \quad (23)$$

$$d_{avg} = \frac{3\sqrt{3}G - 2\pi}{6\sqrt{3}G - 2\pi} \quad (24)$$

When Z-source inverter operates under boost mode, $d_{ST}(\omega t) \geq 0$. So G should be larger than 1.27 from (23) and (24).

Fig.11 shows the switching state of improved PWM strategy (IPWM) for Z-source inverter in the first sextant. The ST interval is symmetrically inserted into the phase-leg of v_{mid} . In the first sextant, the output three-phase voltage meet $v_{max} = v_{ao}$, $v_{mid} = v_{bo}$, $v_{min} = v_{co}$. The thick shaded part represents the ST interval, which serves to regulate the intermediate dc-link voltage ($\langle v_{dc_link} \rangle_{T_s} = v_{ao} - v_{co}$). The active voltage vectors (110, 100) are implemented during non- ST interval to regulate v_{bo} . For symmetry, the switching states in other sextants can be obtained similarly. Since only power devices in one phase leg operate at high switching frequency, IPWM+1P ST can minimize the equivalent switching frequency of power devices in the inverter bridge. As a result, it can be predicted that the switching loss will be reduced to a great extent. As shown in

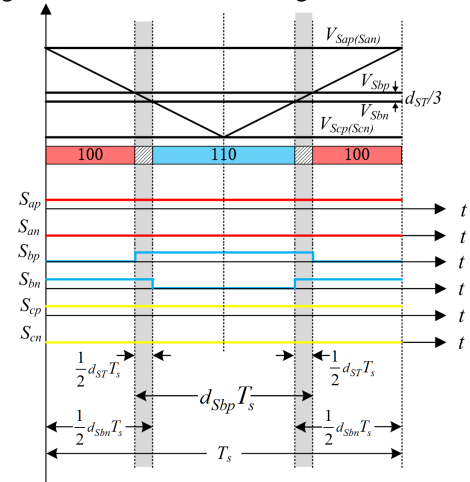


Fig.11 Switching states of Z source inverter with improved PWM strategy in the first sextant.

Fig.11, according to volt-second balance principle, the duty ratio of upper switch d_{Sip} and lower switch d_{Sin} , output voltage of phase-B v_{mid} meet:

$$\begin{cases} v_{mid}(\omega t) - v_{min}(\omega t) = (d_{Sbp}(\omega t) - d_{ST}(\omega t)) \cdot (2V_C - V_{dc}) \\ d_{Sbn}(\omega t) = 1 - d_{Sbp}(\omega t) + d_{ST}(\omega t) \end{cases} \quad (25)$$

Furthermore, $\langle v_{dc_link} \rangle_{Ts}$ is controlled the same as maximum value of three-phase line voltage.

$$(1 - d_{ST}(\omega t)) \cdot (2V_C - V_{dc}) = v_{max}(\omega t) - v_{min}(\omega t) \quad (26)$$

Combining (24) (25) and (26), the corresponding duty ratio expressions of the upper and lower switches d_{Sip} , d_{Sin} in (16) can be modified as:

$$\begin{cases} d_{Sip}(\omega t) = \frac{v_i(\omega t) - v_{min}(\omega t)}{v_{max}(\omega t) - v_{min}(\omega t)} \cdot (1 - d_{ST}(\omega t)) + d_{ST}(\omega t) \\ d_{Sin}(\omega t) = 1 - d_{Sip}(\omega t) + d_{ST}(\omega t) \end{cases} \quad (27)$$

Like the typical PWM strategies of Z-source inverter, IPWM+1P ST can be obtained by the level shift of conventional three-phase VSI modulation waveforms. Fig.12 shows the equivalent carrier wave based PWM and switching state for IPWM + 1P ST. Six modulation waveforms are compared with the triangular wave to produce the gate signals for switches in Z-source inverter. Assume the amplitude of triangular wave is normalized, the modulation waveform expressions of six switches are expressed as follows.

$$\begin{cases} V_{max_Sp}(\omega t) = V_{max_Sn}(\omega t) = 1 \\ V_{mid_Sp}(\omega t) = V_{mid}^*(\omega t) + \frac{1}{2}d_{ST}(\omega t) \\ V_{mid_Sn}(\omega t) = V_{mid}^*(\omega t) - \frac{1}{2}d_{ST}(\omega t) \\ V_{min_Sp}(\omega t) = V_{min_Sn}(\omega t) = 0 \end{cases} \quad (28)$$

Where: V_{max}^* , V_{mid}^* , V_{min}^* refer to the modulation waveforms of conventional three-phase VSI in (5). $V_{Sap}=V_{max_Sp}$, $V_{San}=V_{max_Sn}$, $V_{Sbp}=V_{mid_Sp}$, $V_{Sbn}=V_{mid_Sn}$, $V_{Scp}=V_{min_Sp}$, $V_{Scn}=V_{min_Sn}$ refers to the modulation waveforms of six switches for IPWM+1P ST shown in Fig.12.

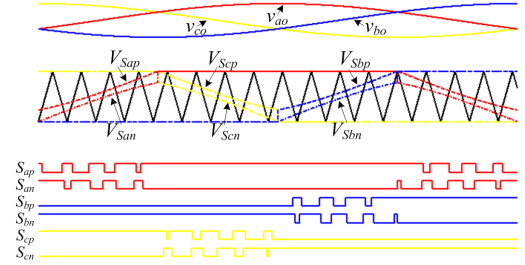


Fig.12 The equivalent carrier-waveform-based PWM for IPWM+1P ST.

IV. COMPARISON OF PWM STRATEGIES

To investigate the inherent advantages and disadvantages of IPWM+1P ST, comparisons with the typical PWM strategies are carried out in terms of voltage boost capability, the requirements of power devices and passive components. According to the operation principle of Z-source inverter using different PWM strategies, the steady-state operation points including voltage gain G , ST interval d_{ST} , capacitor voltage V_C and inductor current I_L can be derived and listed in Table.II. The voltage gain comparison of Z-source inverter with different PWM strategies is shown in Fig.13. Due to full utilization of intermediate dc-link voltage, IPWM+1P ST and MPWM+1P/3P ST have the maximum voltage boost capability.

TABLE II
THE EXPRESSIONS OF VOLTAGE GAIN, FOR Z SOURCE INVERTER WITH DIFFERENT PWM STRATEGIES.

Modulation Scheme	SCPWM + 1P ST [3], SCPWM + 3P ST [3],	MCPWM + 1P ST [17], MCPWM + 3P ST [17],	MPWM + 1P ST [16] MPWM + 3P ST [16] IPWM + 1P ST
Voltage gain (G)	$G = \frac{1-d_{ST}}{1-2d_{ST}} = \frac{M_i}{2M_i-1}$	$G = \frac{2}{\sqrt{3}} \frac{1-d_{ST}}{1-2d_{ST}} = \frac{M_i}{\sqrt{3}M_i-1}$	$G = \frac{2\pi}{3\sqrt{3}} \frac{1-d_{avg}}{1-2d_{avg}} = \frac{\pi M_i}{3\sqrt{3}M_i-\pi}$
ST interval (d_{ST} or d_{avg})	$d_{ST} = 1 - M_i = \frac{G-1}{2G-1}$	$d_{ST} = 1 - \frac{\sqrt{3}}{2} M_i = \frac{\sqrt{3}G-2}{2\sqrt{3}G-2}$	$d_{avg} = 1 - \frac{3\sqrt{3}}{2\pi} M_i = \frac{3\sqrt{3}G-2\pi}{6\sqrt{3}G-2\pi}$
Modulation index (M_i)	$M_i = 1 - d_{ST} = \frac{G}{2G-1}$	$M_i = \frac{2}{\sqrt{3}} (1-d_{ST}) = \frac{G}{\sqrt{3}G-1}$	$M_i = \frac{2\pi}{3\sqrt{3}} (1-d_{avg}) = \frac{\pi G}{3\sqrt{3}G-\pi}$
Capacitor Voltage (V_C)	$V_C = \frac{1-d_{ST}}{1-2d_{ST}} V_{dc} = G V_{dc}$	$V_C = \frac{1-d_{ST}}{1-2d_{ST}} V_{dc} = \frac{\sqrt{3}G}{2} V_{dc}$	$V_C = \frac{1-d_{avg}}{1-2d_{avg}} V_{dc} = \frac{3\sqrt{3}G}{2\pi} V_{dc}$
Inductor current (I_L)	$i_L = \frac{3}{4} \hat{G} \hat{i}_{ac} = \frac{3}{4} \frac{1-d_{ST}}{1-2d_{ST}} \hat{i}_{ac}$	$i_L = \frac{3}{4} \hat{G} \hat{i}_{ac} = \frac{3}{2\sqrt{3}} \frac{1-d_{ST}}{1-2d_{ST}} \hat{i}_{ac}$	$i_L = \frac{3}{4} \hat{G} \hat{i}_{ac} = \frac{\pi}{2\sqrt{3}} \frac{1-d_{avg}}{1-2d_{avg}} \hat{i}_{ac}$

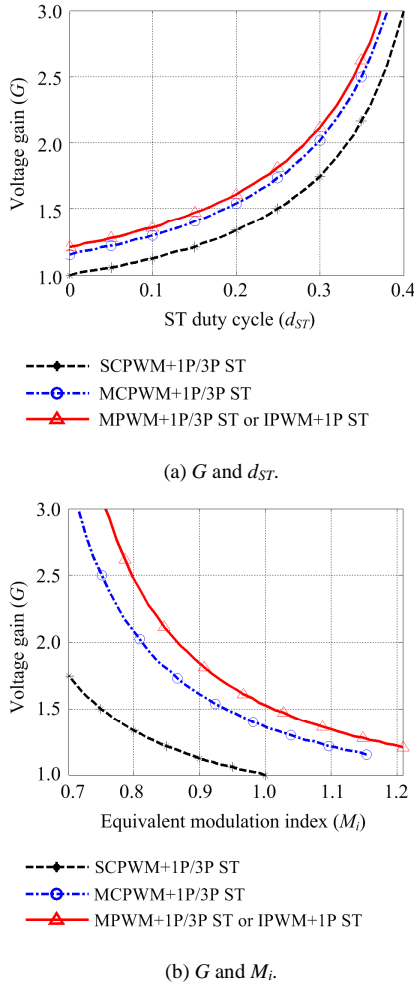


Fig.13 Voltage gain of Z source inverter with different modulation strategies.

A. Power Devices Comparison.

As for Z-source inverter using SCPWM+1P ST and MCPWM+1P ST shown in Fig.5, the switching frequency of power devices in the inverter bridge and D_0 are f_s and $6f_s$ ($f_s=1/T_s$), respectively. For Z-source inverter using MPWM+1P ST shown in Fig.7, the switching frequency of power devices in the inverter bridge and D_0 are $2/3f_s$ and $4f_s$ respectively. IPWM+1P ST uses single-phase leg for ST current conduction without introducing an additional switching communication, which is different from the existing PWM strategies. The equivalent switching frequency is reduced to $1/3f_s$, which is the minimum value among the existing PWM strategies. Table.III lists the equivalent switching frequency of power devices for Z source inverter with different PWM strategies ($f_s=1/T_s$).

According to the operation principle of Z-source inverter, D_0 and switching devices in the inverter bridge withstand the same voltage stress, which is the maximum of intermediate dc-link voltage in (29).

$$v_s = 2V_C - V_{dc} \quad (29)$$

For existing PWM strategies and IPWM, substituting V_C listed in Table.II into (29), the voltage stress of power devices as function of voltage gain G can be derived as follows:

TABLE III

THE EQUIVALENT SWITCHING FREQUENCY OF POWER DEVICES FOR Z SOURCE INVERTER WITH DIFFERENT PWM STRATEGIES ($f_s=1/T_s$).

Modulation Scheme	Switching frequency	
	Front Diode	Switches in inverter bridge
SCPWM + 3P ST, MCPWM + 3P ST [17]	$2f_s$	$2f_s$
SCPWM + 1P ST, MCPWM + 1P ST [17]	$6f_s$	f_s
MPWM + 3P ST [16]	$2f_s$	$4f_s/3$
MPWM + 1P ST [16]	$4f_s$	$2f_s/3$
NPWM + 1P ST	$2f_s$	$f_s/3$

$$v_s = (2G-1)V_{dc} \quad (\text{SCPWM+1P/3P ST}) \quad (30)$$

$$v_s = \frac{\sqrt{3}G-2}{2}V_{dc} \quad (\text{MCPWM+1P/3P ST}) \quad (31)$$

$$v_s = \frac{3\sqrt{3}G-2\pi}{2\pi}V_{dc} \quad (\text{MPWM+1P/3P ST or IPWM+1P ST}) \quad (32)$$

Fig.14 shows the power devices voltage stress comparison for Z-source inverter with different PWM strategies. Maximum boost control strategies (IPWM+1P ST and MPWM+1P/3P ST) have the minimum voltage stress of power devices.

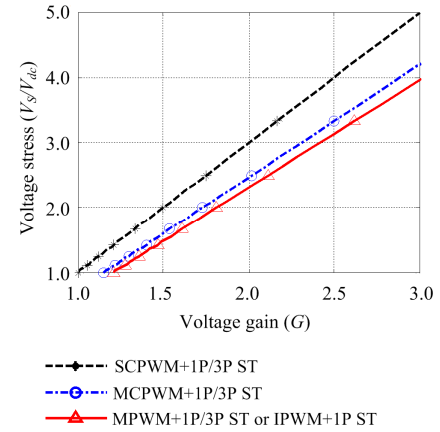


Fig.14 Voltage stress of power device for Z-source inverter with different PWM strategies.

In addition to voltage stress, another key parameter for the selection of power device is the current stress (I_s). Three typical indicators reflecting power device current stress are (a) I_{s_peak} the maximum instant current flowing through the power device defined as (33); (b) I_{s_avg} the average current flowing through power device in each output line-frequency period defined as (34); (c) I_{s_rms} the root mean square (RMS) value of current flowing through power device in each output line-frequency period defined as (35) [32].

$$I_{s_peak} = \max(i_s(\omega t)) \quad (33)$$

$$I_{s_avg} = \frac{1}{2\pi} \left[\int_0^{2\pi} d_{ST}(\omega t) i_{s_ST}(\omega t) d(\omega t) + \int_0^{2\pi} d_{NST}(\omega t) i_{s_NST}(\omega t) d(\omega t) \right] \quad (34)$$

$$I_{S_rms} = \sqrt{\frac{1}{2\pi} \left[\int_0^{2\pi} d_{ST}(\omega t) i_{ST}^2(\omega t) d(\omega t) + \int_0^{2\pi} d_{NST}(\omega t) i_{NST}^2(\omega t) d(\omega t) \right]} \quad (35)$$

According to the definition in (33) (34) and (35), the average and RMS current calculation depends on the on-state duty ratio and current across power device. The mathematic expressions of on-state duty ratio and on-state current in different switching states are derived in the appendix. Then, it is easier to use numerical calculation to get the comparison results.

Figs.15, 16 and 17 show the current stress of IGBT, free-wheeling diode and D_0 for Z-source inverter with different PWM strategies, respectively. The load power factor is unit one here ($\cos(\varphi)=1$). As shown in Fig.15 (a), MCPWM+3P ST and MPWM+3P ST have the minimum peak current. It is because

the large ST current is simultaneously distributed among three-phase legs. Compared with MCPWM+1P ST and MPWM+1P ST, IPWM+1P ST is beneficial to reduce IGBT peak current. This is because the ST interval is inserted in the phase of v_{mid} . As is shown in Fig15.(b), all these PWM strategies have almost the same average current stress of IGBT. This is because eventually the ST current is averagely distributed among three-phase legs in each output line-frequency period. ($T_{line}=1/f_{line}$). When it comes to RMS current of IGBT, PWM with three-phase legs ST (MCPWM+3P ST, MPWM+3P ST) have the minimum value compared with those with single-phase leg ST (MCPWM+1P ST, MPWM+1P ST, IPWM+1P ST). IPWM+1P ST has a little smaller value of RMS current than that of MCPWM+1P ST, MPWM+1P ST.

As shown in Fig.16 (a), maximum boost control strategies (MPWM+1P/3P ST, IPWM+1P ST) have the minimum peak

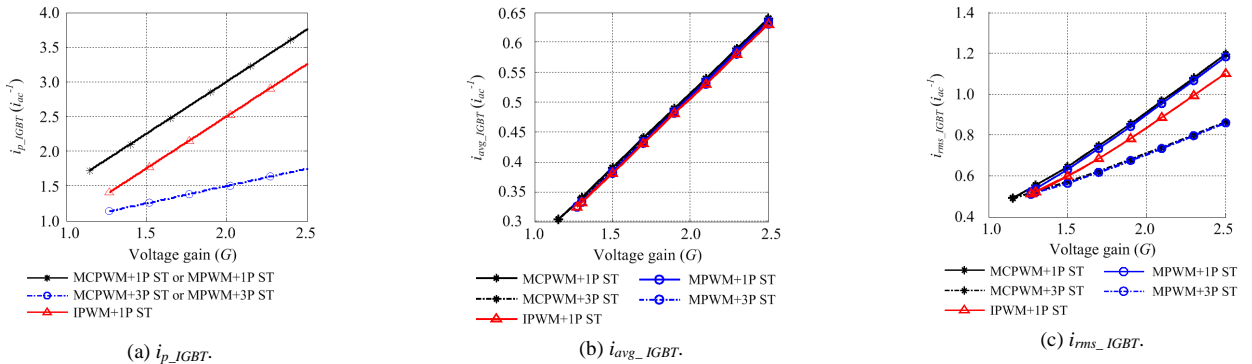


Fig.15 The current stress of IGBT ($\cos(\varphi)=1$).

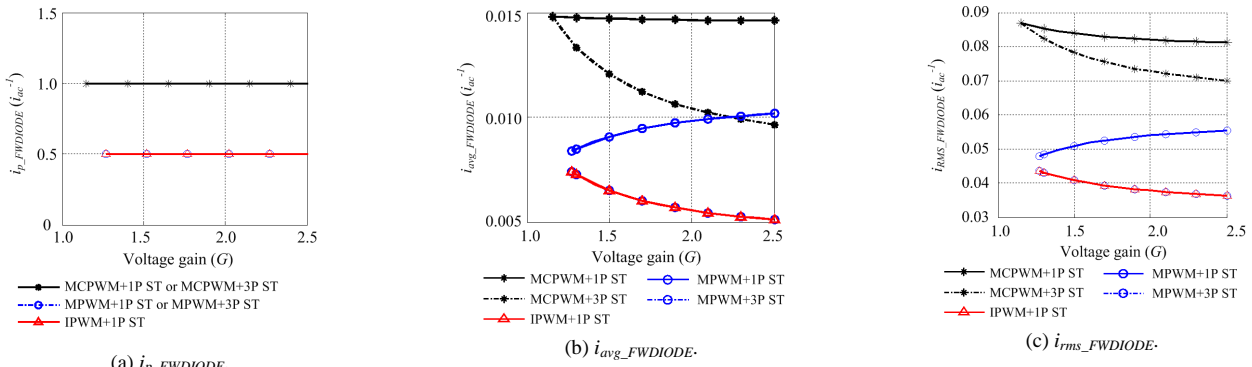


Fig.16 The current stress of free-wheeling diode ($\cos(\varphi)=1$).

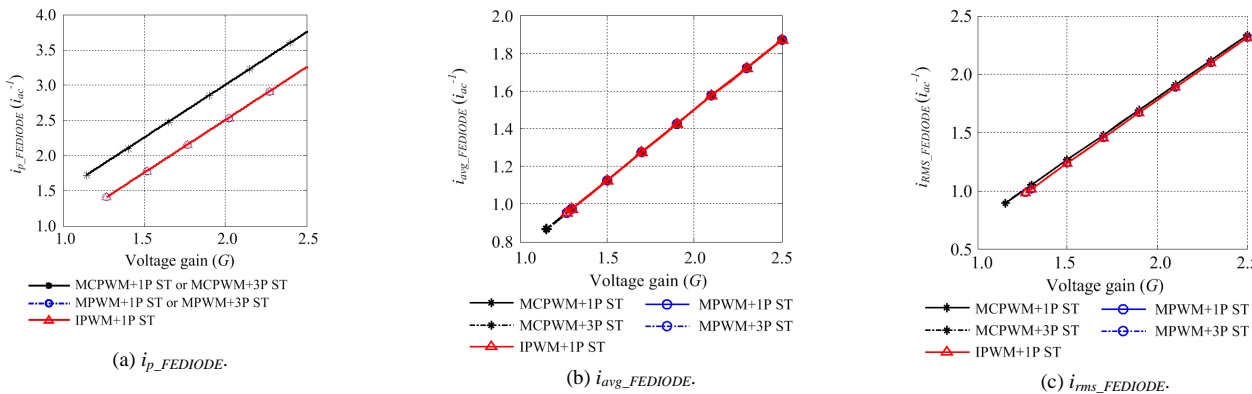


Fig.17 The current stress of front-end diode ($\cos(\varphi)=1$).

current shown in Fig.16.(b) and Fig.16(c). When Z-source inverter supplies three-phase load with high load power factor, current of free-wheeling diode, which is half of maximum constant boost control (MCPWM+1P/3P ST). MPWM+3P ST and IPWM+1P ST have the minimum average current and *RMS* the average and *RMS* current of free-wheeling diode become far smaller than that of IGBT.

As shown in Fig.17, maximum boost control strategies (MPWM+1P/3P ST, IPWM+1P ST) have the minimum value of peak current for D_0 . With different PWM strategies, the average current flowing through D_0 is the input current under certain output power. Thus, they have the same value of average current shown in Fig.17(b). Compared with maximum constant boost control strategies (MCPWM+1P/3P ST), maximum boost control strategies (MPWM+1P/3P ST, IPWM+1P ST) have a little smaller value of *RMS* current.

In all, for Z-source inverter, PWM strategies with different ST injection methods mainly affect the current stress of IGBT, but have little influence on the average and *RMS* current of free-wheeling diode and the front-end diode. Z-source inverter with IPWM+1P ST demonstrates the maximum voltage boost capability, minimum voltage stress and minimum switching frequency of power devices.

B. Passive components requirement comparison.

In general, the cost and volume of passive component is proportional to the available energy stored in it. The inductor core and winding are designed on the basis of the inductance requirement (L) and average current level (I_L) under maximum operation conditions. The inductance is selected to limit the current ripples in a certain range. The capacitor is designed based on the current capacity, capacitance requirement and terminal voltage [27]. The current capacity usually refers to the *RMS* value of the current ripples, which is related the capacitor working temperature and service life. The capacitance is selected according to the limitations of the voltage ripple. The current/voltage ripples of inductor/capacitor are defined as:

$$\Delta I_L = \delta_L \cdot I_L \quad (36)$$

$$\Delta V_C = \delta_C \cdot V_C \quad (37)$$

Where δ_L and δ_C are the ripples coefficients preset based on the performance indices of power converter.

As for maximum constant boost control (MCPWM+1P/3P ST), d_{ST} in one switching time period is constant. Thus, in theory, passive components just contain switching-frequency ripples, which are analyzed in one switching time period T_s . I_L increases during ST interval and decreases during non-ST interval. However, v_C is decreases during ST interval and increases during non-ST interval.

With maximum boost control strategies (MPWM+1P/3P ST, IPWM+1P ST), d_{ST} expressed in (22) keeps changing in each sextant. The typical waveforms of inductor current and capacitor voltage for Z-source inverter are shown in Fig.18. In which, $\langle v_L \rangle_{T_s}$ is the average value of inductor terminal voltage in one switching time period, and $\langle i_C \rangle_{T_s}$ is the average value of capacitor current in one switching time period. In theory,

besides the switching frequency ripples, the passive components also contain six-time-line -frequency ripples, which are analyzed in one sextant. Usually, the amplitude of switching frequency ripples is much smaller than that of six-times line frequency ripples. Thus, the inductance and capacitance in Z-source network should be designed to limit the low-frequency ripples in the desired range. As shown in Fig.18, i_L increases and v_C decreases during II interval ($\omega t_1, \omega t_2$). According to inductor's V-I characteristic, ΔI_L can be calculated by integrating $\langle v_L \rangle_{T_s}$ from ωt_1 to ωt_2 . Similarly, Δv_C can be derived by integrating $\langle i_C \rangle_{T_s}$ from ωt_1 to ωt_2 . The detailed derivation process is in the appendix. Table.IV lists the expressions of inductance and capacitance requirement for Z-source inverter with different PWM strategies.

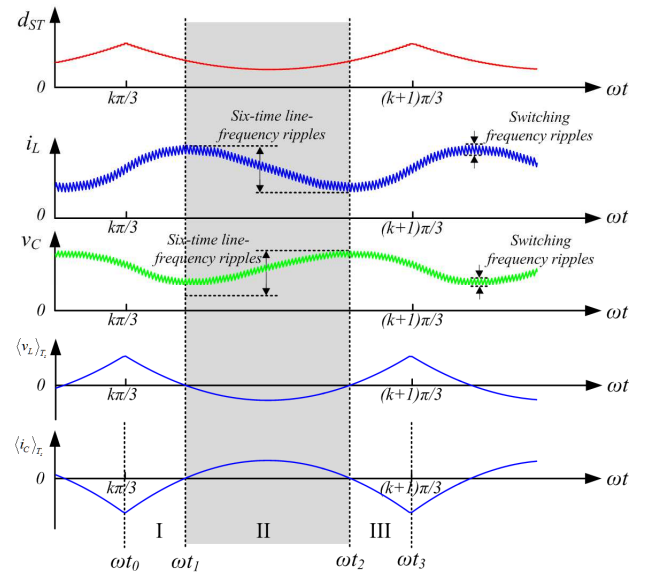


Fig.18 Inductor current and capacitor voltage waveforms for Z-source inverter with maximum boost control strategies (MPWM+1P/3P ST or IPWM+1P ST).

For Z-source inverter with the different PWM strategies, the current of capacitor keeps changing periodically in every sextant. Thus, the *RMS* current of capacitor can be calculated by integrating i_C in 60 degrees. The expressions of duty ratio and capacitor current in different switching states are derived in the appendix.

$$I_{C_rms}^2 = \frac{6}{T_{Line}} \sum \Delta(t) \cdot i_C^2(t) \\ = \frac{3}{\pi} \left[\int_0^{\pi/3} (d_{ST}(\omega t) \cdot (i_C(\omega t))^2 + d_{NST}(\omega t) \cdot (i_C(\omega t))^2) d(\omega t) \right] \quad (38)$$

Based on the equations listed in Table IV and the aforementioned definitions, the relationship of passive components requirements versus voltage gain for Z-source inverter with different PWM strategies are shown in Figs.19 and 20. f_s/f_{line} is the ratio of switching frequency over the output voltage line frequency. The parameters K_L , K_C and K_{C_rms} are defined as:

TABLE IV.
THE EXPRESSIONS OF PASSIVE COMPONENTS REQUIREMENT FOR Z-SOURCE INVERTER WITH DIFFERENT PWM STRATEGIES.

Modulation Scheme	Inductance (L)	Capacitance (C)
MCPWM+3P ST [17]	$L = \frac{1}{2\sqrt{3}} \cdot \frac{\sqrt{3}G-2}{\sqrt{3}G-1} \cdot \frac{V_{dc}}{\delta_L \cdot f_s \cdot \hat{i}_{ac}}$	$C = \frac{\sqrt{3}}{8} \cdot \frac{\sqrt{3}G-2}{\sqrt{3}G-1} \cdot \frac{\hat{i}_{ac}}{\delta_c \cdot f_s \cdot V_{dc}}$
MCPWM+1P ST [17]	$L = \frac{1}{6\sqrt{3}} \cdot \frac{\sqrt{3}G-2}{\sqrt{3}G-1} \cdot \frac{V_{dc}}{\delta_L \cdot f_s \cdot \hat{i}_{ac}}$	$C = \frac{1}{8\sqrt{3}} \cdot \frac{\sqrt{3}G-2}{\sqrt{3}G-1} \cdot \frac{\hat{i}_{ac}}{\delta_c \cdot f_s \cdot V_{dc}}$
MPWM+1P/3P ST [16] IPWM+1P ST	$L = \frac{0.0181}{\sqrt{3}\pi} \cdot \frac{V_{dc}}{\delta_L \cdot f_{line} \cdot \hat{i}_{ac}}$	$C = \frac{0.0181G}{4(3\sqrt{3}G-\pi)} \cdot \frac{\hat{i}_{ac}}{\delta_c \cdot f_{line} \cdot V_{dc}}$

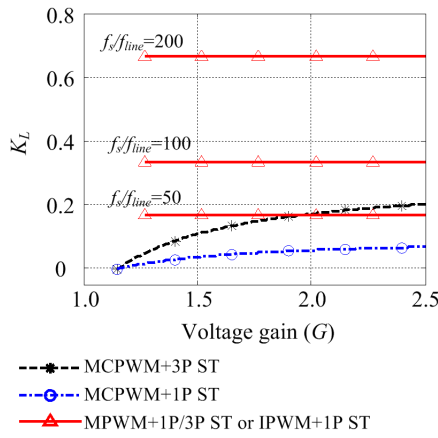


Fig.19 Inductance requirement of Z-source inverter with different PWM strategies.

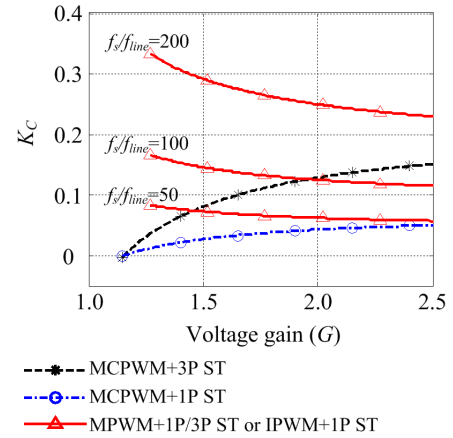
$$K_L = \frac{L}{V_{dc} / \delta_L f_s \hat{i}_{ac}} \quad (39)$$

$$K_C = \frac{C}{\hat{i}_{ac} / \delta_c f_s V_{dc}} \quad (40)$$

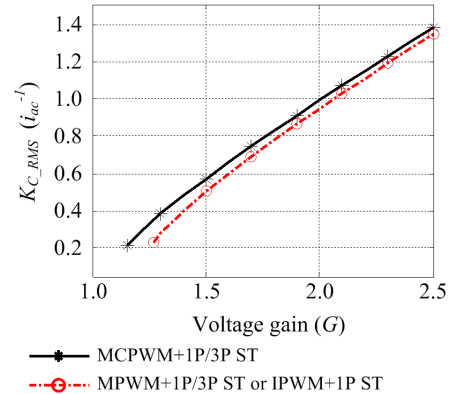
$$K_{IC} = \frac{I_{C_rms}}{\hat{i}_{ac}} \quad (41)$$

Where: K_L reflects the inductance requirement; and K_C , K_{IC} reflect the capacitance requirement and current ripples of capacitor.

Based on the equations listed in Table II, under the same input and output operation condition, Z-source inverter with different PWM strategies has the same average current i_L . With maximum boost control strategies (MPWM+1P/3P ST and IPWM+1P ST), it has the minimum capacitor voltage v_C . As shown in Figs.19 and 20, MCPWM+1P ST has the least inductance and capacitance requirement. With the increase of switching frequency, MCPWM+1P/3P ST needs much smaller inductance and capacitance, compared with MPWM+1P/3P ST and IPWM+1P ST. However, much high switching frequency causes large switching losses of power devices. The tradeoff between the size of passive components and power devices loss should be considered in practical application. Compared with MCPWM+1P/3P ST, MPWM+1P/3P ST and IPWM+1P ST reduce the RMS value of capacitor current ripples.



(a) Capacitance comparison.



(b) RMS current of capacitor.

Fig.20 Capacitor requirement of Z-source inverter with different PWM strategies.

V. CLOSED-LOOP CONTROLLER DESIGN

When Z-source inverter operates with constant boost control, there are two control variables: d_{ST} and M_i . The intermediate capacitor voltage v_C is controlled by d_{ST} and the output ac voltage is controlled by M_i , using separate controllers [27][29]. However, when Z-source inverter operates with maximum boost control (IPWM+1P ST), there is only one control freedom d_{ST} for both regulation of v_C and \hat{v}_{ac} . Fig.21 shows the closed-loop control system diagram, which consists of the dc-side dual-loop

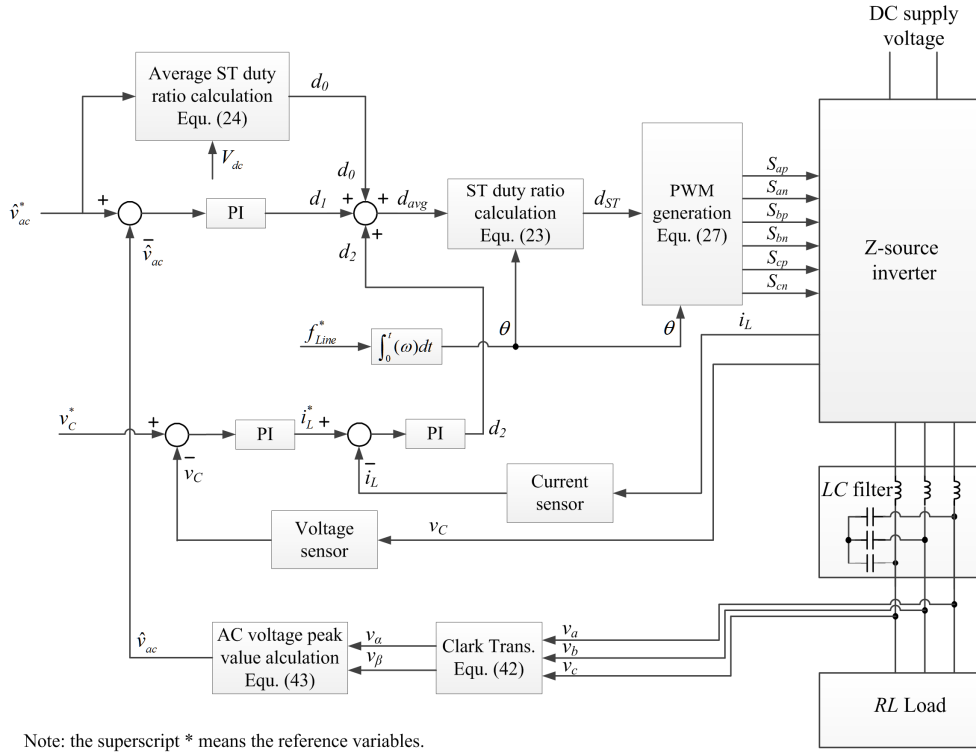


Fig.21 Control system diagram of Z-source inverter with IPWM+1P ST.

capacitor voltage control and the ac-side output voltage control. For a given output voltage reference \hat{v}_{ac}^* , voltage gain G and reference capacitor voltage v_C^* are calculated by (6) and (22). With regarding to the nonlinear relationship of G and d_{avg} expressed in (24) and non-minimum phase characteristics of v_C and d_{avg} in (20), the feed-forward control technique with \hat{v}_{ac}^* and input voltage V_{dc} is introduced to calculate the approximate value of average ST duty ratio d_0 by (24). This is beneficial to achieve a good transient performance. For ac-side control, the amplitude of three-phase voltage is feedback because it is dc component. v_{ao} , v_{bo} , v_{co} are measured and transformed into v_α and v_β in two-axis stationary reference frame according to (42).

$$\begin{bmatrix} v_\alpha \\ v_\beta \end{bmatrix} = \frac{2}{3} \cdot \begin{bmatrix} 1 & -\frac{1}{2} & -\frac{1}{2} \\ 0 & \frac{\sqrt{3}}{2} & -\frac{\sqrt{3}}{2} \end{bmatrix} \cdot \begin{bmatrix} v_a \\ v_b \\ v_c \end{bmatrix} \quad (42)$$

Where: factor $2/3$ is included which means that the amplitude of voltage vector equals to the peak value of the output phase voltage. Then \hat{v}_{ac} can be calculated by:

$$\hat{v}_{ac} = \sqrt{v_\alpha^2 + v_\beta^2} \quad (43)$$

The PI controller output d_1 makes sure three-phase output voltage follows the reference with zero steady-state error. The PI controller output d_2 drives the dc-side capacitor voltage to follow V_C^* . The phase angle θ determines which sextant the

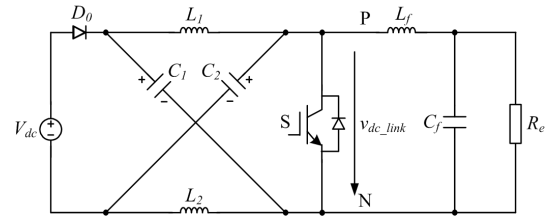


Fig.22 The dc-side equivalent circuit.

reference voltage vector is located in. The instantaneous ST duty ratio d_{ST} is calculated based on d_{avg} and θ according to (23). Then, the PWM module generates PWM signals for six power devices in Z-source inverter according to (27).

The state-space averaged model provides good understanding of circuit characteristic and tools for parameters design of PI controller. For Z-source inverter supplying three-phase balanced load, the ac-side can be transferred to dc-side and simplified as a resistive load connected with an essential LC filter. Fig.22 shows the dc-side equivalent circuit. The equivalent load resistor is calculated based on power balance.

$$R_e = \frac{18}{\pi^2} \cdot R_L \quad (44)$$

By taking all the inductor current (i_L , i_{Lf}) and capacitor voltage (v_C , v_{Cf}) as the state variables and using the state-space averaging method in one switching time period (T_s), the state equations of dc-side equivalent circuit can be expressed as (45).

0885-8993 (c) 2016 IEEE. Personal use is permitted, but republication/redistribution requires IEEE permission. See http://www.ieee.org/publications_standards/publications/rights/index.html for more information.

VI. SIMULATION AND EXPERIMENT VERIFICATION

Numerical simulations using MATLAB/Simulink have been performed to verify IPWM+1P ST and theoretical analysis. The main circuit parameters are: $V_{dc}=300\sim400V$, $L=8mH$, $C_1=C_2=330\mu F$, $L_f=400\mu H$, $C_f=25\mu F$, $R_{Load}=60\Omega$, $L_{load}=2mH$. The switching time period T_s is $100\mu s$. The output line frequency is $f_{line}=50Hz$. The current/voltage ripple coefficients of inductor/capacitor for Z-source network are preset as $\delta_L = 0.4$, $\delta_C = 0.0015$ under the maximum operation condition $G=2.1$, $i_L=10A$, $V_C=600V$. The cutoff frequency of low pass filter in output side is set about $2kHz$ ($f_c=1/5f_s$) to attenuate the

switching frequency ripples.

Fig.24 shows the captured waveforms of Z-source inverter with IPWM+1P ST under the output reference voltage of $\hat{v}_{ac} = 310V$. According to (6) and (22), the voltage gain $G=1.56$, the capacitor voltage $V_C=514.6$ calculated in theory are identical to the simulation results. Compared with the existing PWM strategies, Z-source inverter with IPWM+1P ST achieves the maximum voltage gain as well as minimum voltage stress and switching frequency of power devices.

A laboratory prototype rated at 2.5 kW was built to confirm the improved PWM strategy with Infineon power devices. Fig.25 shows a photograph of the test platform. The main

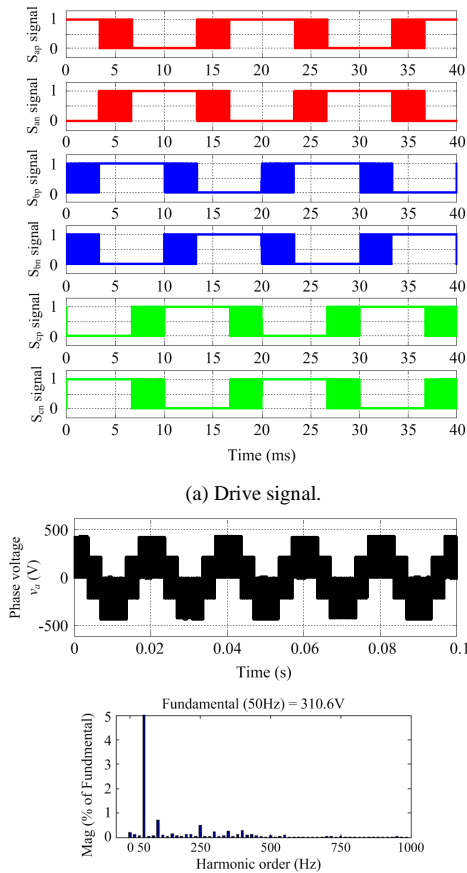


Fig.24 Simulation results for Z-source inverter with IPWM + 1P ST.

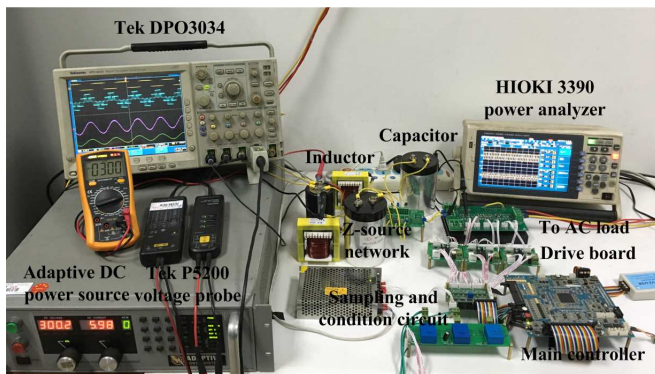


Fig.25 Z-source inverter test platform.

control board is designed based on DSP28335. The drive circuit of IGBT is designed with ACPL-330J based on the existing mature technology. A programmable dc power supply is arranged as the dc source to simulate the V-I characteristics of fuel cells and solar arrays. A Y-type three-phase RL load is connected to the ac side of the inverter. HIOKI 3390 power analyzer simultaneously measures the input DC power and AC output power to perform efficiency analysis. The time duration of each switching instant is pre-calculated in DSP28335. The conditioning board performs logic operations to generate gate signals of power devices according to the requirement of the output voltage vector. The specifications for the experimental

prototype are listed in Table V. The key parameters of closed-loop controllers are $G_{i_L}(z) = 0.11 + 0.0035 \cdot z/(z-1)$; $G_{v_c}(z) = 0.06 + 0.012 \cdot z/(z-1)$; $G_{v_{qf}}(z) = 0.048 + 0.03 \cdot z/(z-1)$.

TABLE V
THE SPECIFICATIONS FOR THE EXPERIMENTAL PROTOTYPE

Switching device	Front-end diode	DIODE (IDP30E120)
	S_{ap} , S_{an} , S_{bp} , S_{bn} , S_{cp} , S_{cn}	IGBT(IGW25N120) and DIODE(IDP18E120)
Passive components	L	8mH
	C_1 and C_2	330uF
Three-phase EMI filter	L_f	400uH
	C_f	35uF
Three-phase RL load	R_{load}	40Ω~300Ω
	L_{load}	2mH
Switching time period	T_s	100us
Current sensor	H_i	0.1
Voltage sensor	H_{v_c} and $H_{v_{qf}}$	0.01

For Z-source inverter with IPWM+1P ST, the inductor current in the impedance network inevitably contains 300Hz low-frequency ripples for 50Hz ac output. Fig.26 shows the frequency characteristic of control to inductor current, intermediate capacitor voltage and filtered output voltage. In order to suppress the undesired influence of low frequency ac

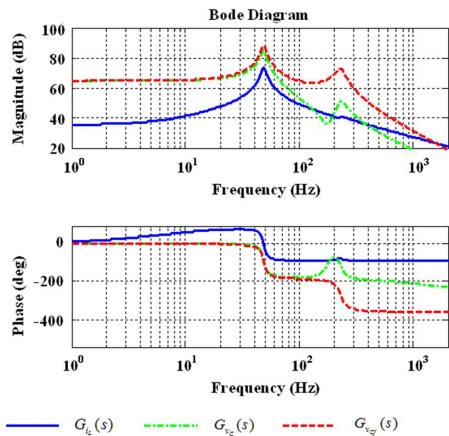


Fig.26 Frequency characteristic of control to inductor current, intermediate capacitor voltage and output voltage.

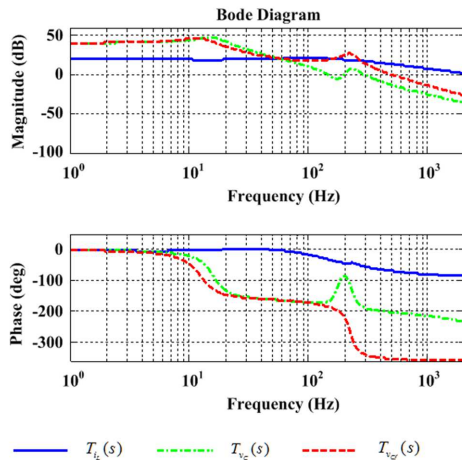
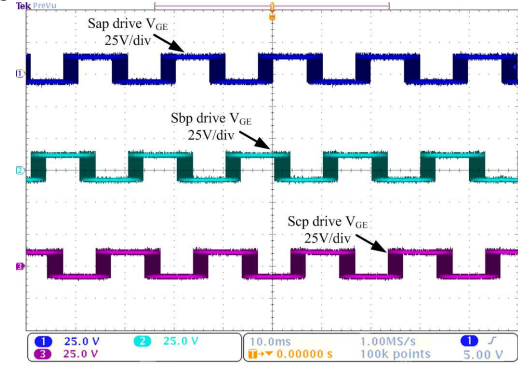


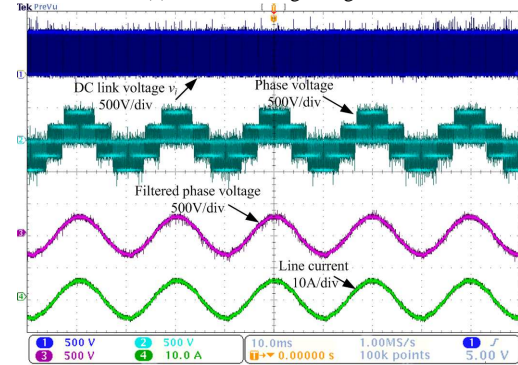
Fig.27 The closed-loop frequency response of inductor current, intermediate capacitor voltage and output voltage.

components, the bandwidth of inner current loop is designed below 300Hz. Fig.27 shows the designed closed-loop frequency responses. The inner current loop is designed with 200Hz bandwidth and 45° phase margin. The intermediate capacitor voltage loop and output voltage loop are designed with almost 25Hz bandwidth and 30° phase margin, which is beneficial to reduce the voltage oscillatory.

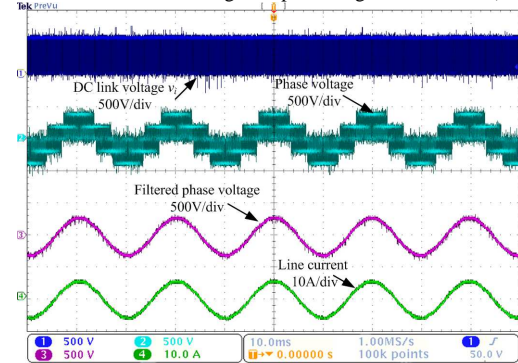
Fig.28 shows the experiment results for Z-source inverter with IPWM+1P ST under the output reference voltage of $\hat{v}_{ac} = 310V$ when the input voltage $V_{dc} = 300V \sim 400V$. The maximum voltage gain of $G = 2.07$ can be obtained. Fig.28(a) shows the voltage waveforms of gate signals for power devices (S_{ap} , S_{bp} , and S_{cp}). During each sextant, the switches in the legs of v_{max} and v_{min} are fixed. Only switches in one phase leg of v_{mid} are commutating with PWM. Fig.28(b) shows the captured waveforms of the intermediate dc-link voltage, the output phase voltage before and after the filter, as well as the output



(a) Power device gate signals.



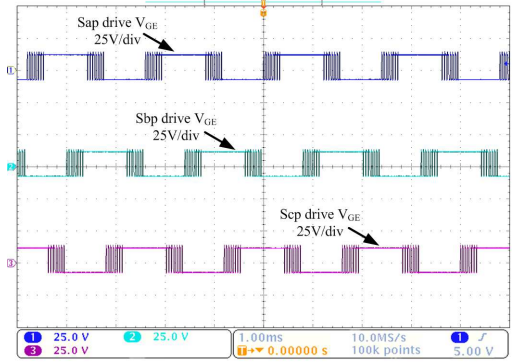
(b) The intermediate dc-link voltage, output voltage, and current. ($V_{dc} = 300V$)



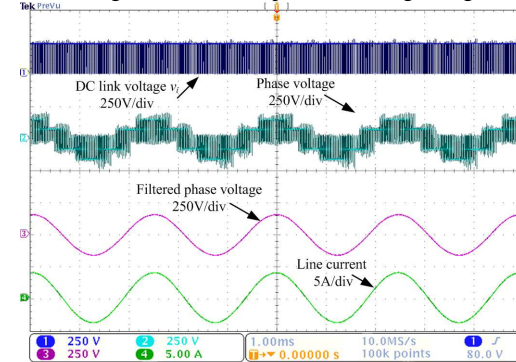
(c) The intermediate dc-link voltage, output voltage, and current. ($V_{dc} = 400V$)
Fig.28 Z-source inverter with IPWM+1P ST ($R_L = 60\Omega$, $f_{line} = 50Hz$).

current. By adjusting the ST to maintain the filtered output phase voltage is 220V/50Hz, the measured intermediate capacitor voltage is about 517.8V, which is a little larger than the theoretical values of 514 V. This is due to the voltage drop and power loss of switches in the inverter bridge. Compared with existing PWM strategies, IPWM+1P ST achieves the minimum intermediate dc-link capacitor voltage and equivalent switching frequency.

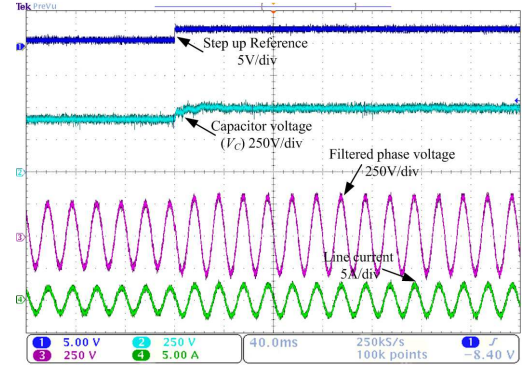
The maximum boost PWM strategy introduces six-time line-frequency ripples in the dc-side inductor current and the capacitor voltage. Therefore, it is more suitable for 400-800Hz medium frequency application of power supply system due to a relatively high output line frequency. Fig.29 shows the captured waveforms for Z-source inverter using IPWM+1P ST when the output phase voltage is 110V/400Hz, The dc source voltage is $V_{dc}=200V$, The switching time period is $T_s=50\mu s$. The maximum voltage gain of $G=1.56$ can be obtained. The measured intermediate capacitor voltage 261.3V is quite consistent with the theoretical value 258V calculated from (22). Fig.30 (a) and (b) show the experimental results when the reference output voltage \hat{v}_{ac}^* has a step change from 250V to 310V and back to 250V respectively. The controller is stable under steady state operation and the step change response is also fast with acceptable response time. With controller design shown in Fig.21, the output three-phase voltage has good transient performance. The output three-phase voltage follows the reference when the intermediate capacitor voltage $V_C=413.5V$ achieves new steady state $V_C=514.4V$. Fig.31(a) and (b) show the experimental results when the load resistance



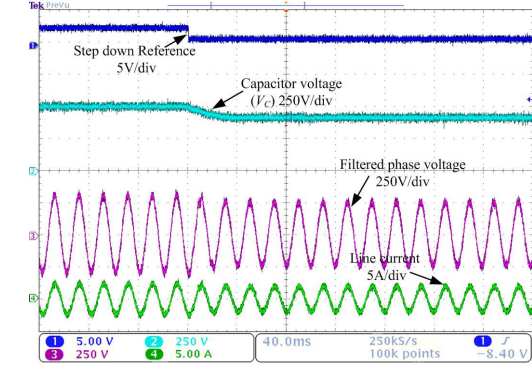
(a) Voltage waveforms of power device gate signals.



(b) The intermediate dc-link voltage, output voltage, and current. ($V_{dc}=200V$)
Fig.29 Z-source inverter with IPWM+1P ST ($V_{dc}=200V$, $R_L=40\Omega$, $f_{line}=400Hz$).

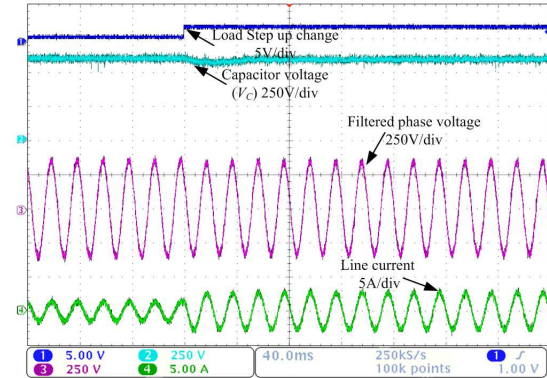


(a) Step up 250V~310V.

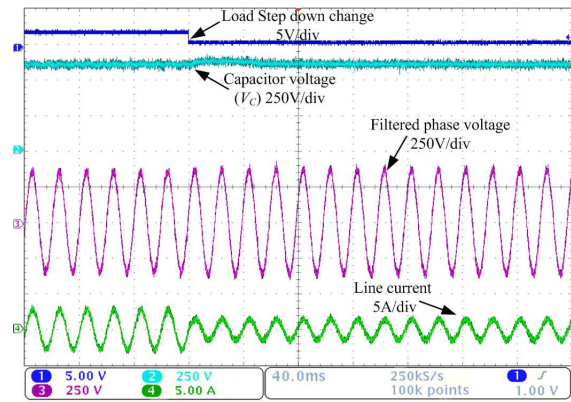


(b) Step down 310V~250V.

Fig.30 Dynamic responses of Z-source inverter under step change of output voltage reference ($V_{dc}=300V$, $R_L=120\Omega$).



(a) Step change of R_L from 160Ω to 120Ω



(b) Step change of R_L from 120Ω to 160Ω

Fig.31 Dynamic responses of Z-source inverter under step change of load resistance ($V_{dc}=300V$, $\hat{v}_{ac}^* = 350V$).

has a step change from $R_L=160\Omega$ to $R_L=120\Omega$ and back to $R_L=160\Omega$ respectively. The dc-side capacitor voltage and output ac voltage recover quickly.

The losses of power converter include semiconductor devices losses, passive components losses, controller and driver losses and etc. Among them, the semiconductor devices losses are the dominant part. IGBT losses consist of turn-on and turn-off switching losses besides conduction losses. DIODE losses include the reverse recovery losses and conduction losses because the turn-on losses are small enough to be neglected [35]. The switching losses model of semiconductor device can be expressed as follows [35]-[37]:

$$E_{sw(on,off)} = (\alpha + \beta \cdot i_{sw} + \gamma \cdot i_{sw}^2) \frac{V_{sw}}{V_{ref}} \quad (53)$$

$$P_{sw} = f_{sw} \cdot (E_{swon} + E_{swoff}) \quad (54)$$

Where: V_{sw} is the blocking voltage; i_{sw} is the switched current; α , β , γ are the device parameters from the datasheet. V_{ref} is the reference voltage under which device parameters are derived.

The conduction losses of the front-end diode and switches in the inverter bridge can be calculated by:

$$P_{con_dc} = \frac{1}{T_s} \int_{t_1}^{t_2} v_{con} \cdot i_{con} dt \quad (55)$$

$$P_{con_inv} = \frac{1}{2\pi} \int_{\lambda_1}^{\lambda_2} d_{con} \cdot v_{on} \cdot i_{con} d\theta_r \quad (56)$$

Where: $v_{con}=v_{th}+ri_{con}$ is on-state voltage drop. v_{th} is threshold voltage; r is on-state resistor. i_{con} is conduction current, d_{con} is conduction duration.

According to the power devices losses model, the switching losses and conduction losses of each power device can be calculated for theoretical analysis. Fig.32 shows the losses distribution of Z-source inverter with different PWM strategies operating at normal condition as a reference. IGBT switching losses and front-end DIODE D_0 reverse recovery losses occupy the main part. Therefore, the reduction of switching frequency and voltage stress is of great importance for efficiency improvement. The conduction loss of free-wheeling Diode is the minor part. All the PWM strategies only have a slight difference in the conduction losses of IGBT and D_0 . This is because by using different PWM strategies, IGBT and D_0 have almost the same average current stress in Fig.15(b) and

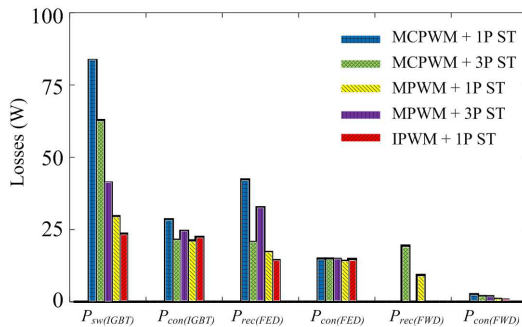
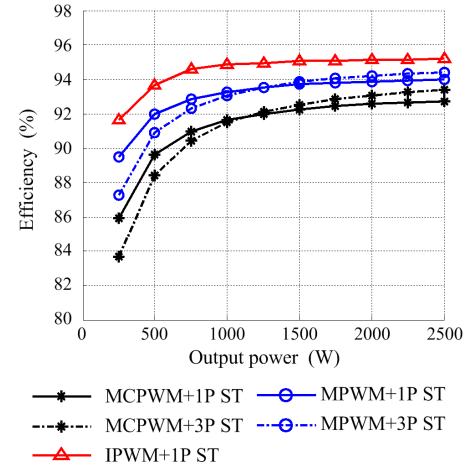


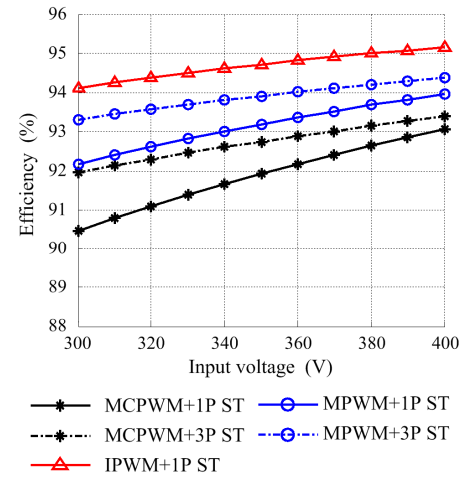
Fig.32 Theoretical analysis of losses distribution for Z-source inverter with different PWM strategies. ($V_{dc}=300V$, $\hat{v}_{ac}=311V$, $P_o=2500W$, $T_s=100\mu s$)

Fig.17(b), respectively. MCPWM+1P ST has the maximum IGBT switching losses due to a larger ST current compared with 3P ST method. Fortunately, for MCPWM+1P ST in Fig.5, MPWM+1P ST in Fig.7 and IPWM+1P ST in Fig.11, the ST interval is inserted at the instants of switching commutation between anti-parallel diode and IGBT. All the freewheeling diodes in the inverter bridge achieve zero voltage turn off. Thus, free-wheeling diodes have almost no reverse recovery losses [34]. The turn on losses of IGBT can be reduced, too. Because the reduced switching frequency of IGBT and the front-end diode contributes to lowering power device losses, IPWM+1P ST achieves the highest efficiency.

In order to quantify the improvement introduced by IPWM+1P ST, the main circuit efficiency of Z-source inverter with different PWM strategies is measured under different output power and input voltage. Fig.33 shows the efficiency comparison results of Z-source inverter operating at (a) $V_{dc}=300V$, $\hat{v}_{ac}=311V$, $P_o=500\sim 2500W$ by the change of load resistance; (b) $V_{dc}=300\sim 400V$, $\hat{v}_{ac}=311V$, $P_o=2500W$ by the



(a) Efficiency versus output power. ($V_{dc}=400V$, $\hat{v}_{ac}=311V$, $P_o=250\sim 2500W$)



(b) Efficiency versus input voltage. ($V_{dc}=300\sim 400V$, $\hat{v}_{ac}=311V$, $P_o=2500W$)

Fig.33 Efficiency comparison of Z-source inverter with different PWM strategies.

change of input voltage. The efficiency is increased with the decrease of voltage gain. Compared with existing PWM strategies, Z-source inverter with IPWM+1P ST demonstrates best efficiency due to the reduced switching frequency and voltage stress of power devices.

VII. CONCLUSION

This paper presents an improved PWM strategy for Z-source inverter, which can minimize the voltage stress and switching frequency of power devices. Simulation and experiment results validate the theoretical analysis. Compared with existing PWM strategies, Z-source inverter with the IPWM demonstrates higher efficiency under full operation range of low voltage gain (1.27~2) application. However, the dc-side inductor current and capacitor voltage contain six-time-line-frequency ripples, which consequently require large size of the passive components when the output frequency is very low. Thus, it is also suitable for 400-800Hz medium frequency aircraft and vessel power supply system due to a relatively high output line frequency. Furthermore, the idea of improved PWM strategy can be extended to other kinds of three-phase impedance network based inverters.

APPENDIX

1) Current stress derivation of IGBT and freewheeling Diode.

Because of the symmetry, each IGBT and freewheeling Diode in the inverter bridge has the same current stress. Thus, only IGBT S_{ap} and Diode D_{an} are analyzed for example.

(1) MCPWM+1P ST.

During ST interval, D_0 is blocked. As shown in Fig.34, i_{Sap} is i_{dc_link} minus i_{bc} . i_{dc_link} is $2i_L$. i_{bc} represents the sum of current across S_{bp} and S_{cp} , which depends on the current and switching states of phase b and c.

$$i_{Sap} = i_{dc_link}(\omega t) - i_{bc}(\omega t) = 2i_L - i_{bc}(\omega t) \quad (57)$$

$$i_{bc} = S_{bp} \cdot i_b(\omega t) + S_{cp} \cdot i_c(\omega t) \quad (58)$$

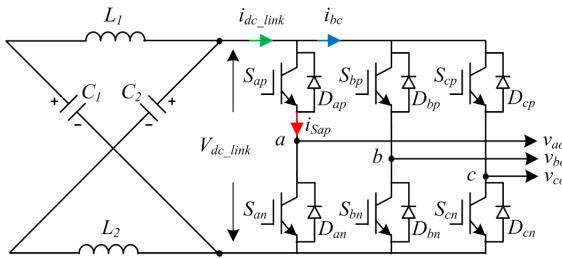


Fig.34 The current of S_{ap} during ST state for PWM strategies with 1P ST.

According to (57) and (58), ST current across S_{ap} in different sextants can be derived as

$$i_{S1(ig)-ST}(\omega t) = \begin{cases} 2i_L & (-\frac{\pi}{3} \leq \omega t \leq \frac{\pi}{3}) \\ 2i_L - i_b(\omega t) & (\frac{\pi}{3} \leq \omega t \leq \frac{\pi}{2}) \\ 2i_L - i_c(\omega t) & (-\frac{\pi}{2} \leq \omega t \leq -\frac{\pi}{3}) \end{cases} \quad (59)$$

From (59), the maximum instant current through S_{ap} occurs

during ST interval $i_{p_IGBT}=2i_L$. The ST interval d_{ST} is obtained from Table.II.

During non-ST interval, S_{ap} and D_{an} conduct when i_a is positive ($-\pi/2 \leq \omega t \leq \pi/2$). The conduction current is i_a . Thus, the maximum instant current through D_{an} is peak value of load current $i_{p_FW_DIODE}=\hat{i}_{ac}$. As shown in Fig.5, the on-state interval of S_{ap} and D_{an} in a half line cycle can be derived as (60) and (61), respectively.

$$d_{Sap(IGBT)-NST}(\omega t) = \begin{cases} V_{Sap(San)}(\omega t) - \frac{d_{ST}(\omega t)}{6} & (\frac{\pi}{3} \leq \omega t \leq \frac{\pi}{2}) \\ V_{Sap(San)}(\omega t) + \frac{d_{ST}(\omega t)}{6} & (-\frac{\pi}{3} \leq \omega t \leq \frac{\pi}{3}) \\ V_{Sap(San)}(\omega t) - \frac{d_{ST}(\omega t)}{6} & (-\frac{\pi}{2} \leq \omega t \leq -\frac{\pi}{3}) \end{cases} \quad (60)$$

$$d_{San(Diode)-NST}(\omega t) = \begin{cases} 1 - d_{Sap(IGBT)-NST}(\omega t) - \frac{d_{ST}(\omega t)}{2} & (-\frac{\pi}{3} \leq \omega t \leq \frac{\pi}{3}) \\ 1 - d_{Sap(IGBT)-NST}(\omega t) - \frac{d_{ST}(\omega t)}{6} & (\frac{\pi}{3} \leq \omega t \leq \frac{\pi}{2}) \\ 1 - d_{Sap(IGBT)-NST}(\omega t) - \frac{d_{ST}(\omega t)}{6} & (-\frac{\pi}{2} \leq \omega t \leq -\frac{\pi}{3}) \end{cases} \quad (61)$$

(2) MPWM+1P ST.

For MPWM+1P ST, the main difference from MCPWM+1P is the periodically varied d_{ST} in (10). D_{an} is always turned off in the first sextant. Thus, the maximum instant current occurs at the beginning of the second sextant. It is half of load peak current $i_{p_FW_diode}=0.5\hat{i}_{ac}$. Substituting (10) into (60) and (61), the key parameters for current stress analysis can be obtained.

(3) IPWM+1P ST.

For IPWM+1P ST, ST interval is inserted in phase a in the second sextant ($\pi/3 \leq \omega t \leq 2\pi/3$). Thus, the maximum instant currents of IGBT and freewheeling Diode occur at the beginning of the second sextant. $i_{p_IGBT}=2i_L - 0.5\hat{i}_{ac}$. $i_{p_FW_diode}=0.5\hat{i}_{ac}$.

(4) MCPWM+3P ST.

For MCPWM+3P ST, during ST interval, all the switches in the inverter bridge are turned on. Assuming the on-state resistors of each switch have the same value shown in Fig.35, the current across S_{ap} and S_{an} meet:

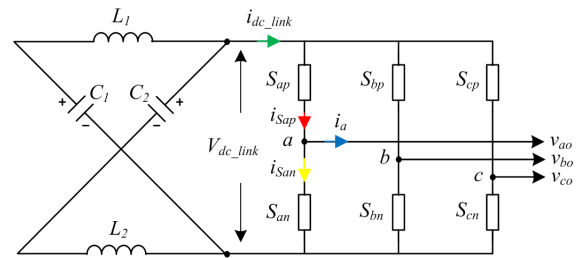


Fig.35 The current of S_{ap} during ST interval for MCPWM+3P ST and MPWM+3P ST.

$$\begin{cases} i_{Sap}(\omega t) + i_{San}(\omega t) = \frac{4}{3}i_L \\ i_{Sap}(\omega t) - i_{San}(\omega t) = i_a(\omega t) \end{cases} \quad (62)$$

From (62), the ST current through S_{ap} can be derived as:

$$i_{Sap}(\omega t) = \frac{2}{3}i_L + \frac{1}{2}i_a(\omega t) \quad (63)$$

From (63), the maximum instant current through IGBT during ST interval is

$$i_{p_IGBT} = \frac{2}{3}i_L + \frac{1}{2}\hat{i}_{ac} \quad (64)$$

Seen from Fig.35, during non-ST interval, the conduction current across S_{ap} and D_{an} is phase current i_a , but the conduction duration of S_{ap} and D_{an} decrease by $d_{ST}/2$ compared with conventional three-phase VSI.

$$d_{Sap_NST}(\omega t) = V_{Sap(San)}^*(\omega t) - \frac{1}{2}d_{ST}(\omega t) \quad (65)$$

$$d_{Dan_NST}(\omega t) = 1 - V_{Sap(San)}^*(\omega t) - \frac{1}{2}d_{ST}(\omega t) \quad (66)$$

(5) MPWM+3P ST.

For MPWM + 3P ST, the key parameters of current stress analysis can be obtained by substituting (10) into (65) and (66). D_{an} is always turned off in the first sextant. Thus, the maximum instant current occurs at the beginning of the second sextant $i_{p_FW_diode} = 0.5\hat{i}_{ac}$.

2) Current stress derivation of the front-end Diode.

As for Z-source inverter, D_0 is conducting during non-ST interval and the equivalent circuit is shown in Fig.36. i_{D0} can be expressed as $2i_L - i_{dc_link}$. In one switching time period, i_{dc_link} changes among zero and different load current.

$$i_{D0_NST}(\omega t) = i_L(\omega t) + i_c(\omega t) = 2i_L(\omega t) - i_{dc_link}(\omega t) \quad (67)$$

$$i_{dc_link}(\omega t) = S_{ap}(\omega t)i_a(\omega t) + S_{bp}(\omega t)i_b(\omega t) + S_{cp}(\omega t)i_c(\omega t) \quad (68)$$

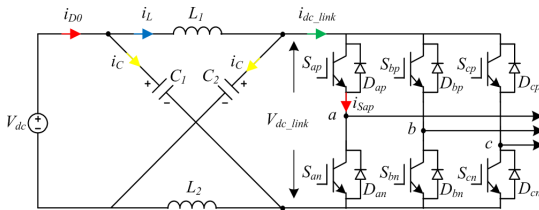


Fig.36 The current analysis of D_0 during non-ST interval.

In the first sextant, i_{D0} in different switching state is:

$$i_{FE(Diode)}(\omega t) = \begin{cases} 2i_L & (111,000) \\ 2i_L - i_a(\omega t) & (100) \\ 2i_L + i_c(\omega t) & (110) \end{cases} \quad (69)$$

The corresponding duty ratio of different switching state is:

$$\begin{cases} d_{(111,000)}(\omega t) = 1 - V_{Sap(San)}^*(\omega t) + V_{Scp(Scn)}^*(\omega t) - d_{ST}(\omega t) & (111,000) \\ d_{(100)}(\omega t) = V_{Sap(San)}^*(\omega t) - V_{Sbp(Sbn)}^*(\omega t) & (100) \\ d_{(110)}(\omega t) = V_{Sbp(Sbn)}^*(\omega t) - V_{Scp(Scn)}^*(\omega t) & (110) \end{cases} \quad (70)$$

With MCPWM+1P ST and MCPWM+3P ST, the peak current of D_0 occurs in zero switching state, which is $2i_L$. With MPWM+1P ST and MPWM+3P ST, there is no zero switching

state in non-ST interval. From (69), the peak current of D_0 is

$$i_{p_FE(Diode)} = 2i_L - \frac{1}{2}i_{ac} = \left(\frac{3}{2}G - \frac{1}{2}\right)i_{ac} \quad (71)$$

With different PWM strategies, the interval of active voltage vectors can be obtained from (70).

3) Passive components ripples derivation.

(1) MCPWM+1P ST and MCPWM+3P ST.

A. Inductor requirement

As shown in Fig.10, during ST interval, $V_L = V_C$ and i_L is increasing. And during non-ST interval, $V_L = V_{dc} - V_C$ and i_L is decreasing. The average voltage across inductor in one switching time period is zero.

For MCPWM+1P ST in Fig.4 and MCPWM+3P ST in Fig.5, each ST interval is $1/2d_{ST}T_s$ and $1/6d_{ST}T_s$, respectively. Thus, the inductor current ripples can be appropriately calculated based on d_{ST} and V_C .

$$\Delta i_L = \frac{1}{L} \cdot V_C \cdot \frac{d_{ST}}{2} T_s \quad \text{For MCPWM+3P ST} \quad (72)$$

$$\Delta i_L = \frac{1}{L} \cdot V_C \cdot \frac{d_{ST}}{6} T_s \quad \text{For MCPWM+1P ST} \quad (73)$$

Substituting V_C and d_{ST} listed in Table.II into (72) and (73), Δi_L can be rewritten as:

$$\Delta i_L = \frac{\sqrt{3} \cdot (\sqrt{3}G - 2)G}{8 \sqrt{3}G - 1} \cdot \frac{V_{dc}}{L f_s} \quad \text{For MCPWM+3P ST} \quad (74)$$

$$\Delta i_L = \frac{\sqrt{3} \cdot (\sqrt{3}G - 2)G}{24 \sqrt{3}G - 1} \cdot \frac{V_{dc}}{L f_s} \quad \text{For MCPWM+1P ST} \quad (75)$$

B. Capacitor requirement

As shown in Fig.10, during ST interval, the discharging current of capacitor is i_L .

$$i_{C_ST}(\omega t) = -i_L \quad (76)$$

The charging current of capacitor during non-ST interval is $i_L - i_{dc_link}$. In which, i_{dc_link} changes among three-phase load current at different switching states. i_{C_NST} in the first sextant is expressed as

$$i_{C_NST}(\omega t) = i_L - i_{dc_link}(\omega t) = \begin{cases} i_L & (111,000) \\ i_L - \hat{i}_{ac} \cos(\omega t) & (100) \\ i_L + \hat{i}_{ac} \cos(\omega t + \frac{2\pi}{3}) & (110) \end{cases} \quad (77)$$

The average current across the capacitor in one switching time period is zero. From (76), the capacitor voltage ripples for MCPWM+1P/3P ST can be calculated based on d_{ST} and i_L .

$$\Delta V_C = \frac{1}{C} \cdot i_L \cdot \frac{d_{ST}}{2} T_s \quad \text{For MCPWM+3P ST} \quad (78)$$

$$\Delta V_C = \frac{1}{C} \cdot i_L \cdot \frac{d_{ST}}{6} T_s \quad \text{For MCPWM+1P ST} \quad (79)$$

Substituting i_L and d_{ST} in Table.II into (78) and (79), the

capacitor voltage ripples can be rewritten as:

$$\Delta V_C = \frac{3}{16} \frac{(\sqrt{3}G-2)G}{\sqrt{3}G-1} \cdot \frac{\hat{i}_{ac}}{Cf_s} \quad \text{For MCPWM+3P ST} \quad (80)$$

$$\Delta V_C = \frac{1}{16} \frac{(\sqrt{3}G-2)G}{\sqrt{3}G-1} \cdot \frac{\hat{i}_{ac}}{Cf_s} \quad \text{For MCPWM+1P ST} \quad (81)$$

Base on (76), (77), the capacitor *RMS* current ripples can be calculated as

$$I_{S_rms}^2 = \frac{6}{T_{Line}} \sum d(t) \cdot i_c^2(t) = \frac{3}{\pi} \int_0^{\pi/3} \left[\begin{aligned} & d_{ST}(\omega t) \cdot (-i_L)^2 + d_{(111,000)}(\omega t) \cdot (i_L)^2 \\ & + d_{(100)}(\omega t) \cdot (i_L - \hat{i}_{ac}(\omega t))^2 \\ & + d_{(110)}(\omega t) \cdot (i_L + \hat{i}_{ac}(\omega t + \frac{2\pi}{3}))^2 \end{aligned} \right] d(\omega t) \quad (82)$$

(2) MPWM+1P ST, MPWM+3P ST and IPWM+1P ST

A. Inductor requirement

The average voltage across the inductor in one switching time period can be derived as:

$$\langle v_L(\omega t) \rangle_{T_s} = V_C \cdot d_{ST}(\omega t)T_s + (V_{dc} - V_C)(1 - d_{ST}(\omega t))T_s \quad (83)$$

Substituting V_C and d_{st} in Table.II into (83), $\langle v_L(\omega t) \rangle_{T_s}$ can be simplified as:

$$\langle v_L(\omega t) \rangle_{T_s} = \frac{\sqrt{3}G}{2} \left[\frac{3}{\pi} - \cos(\omega t - \frac{\pi}{6}) \right] \quad (84)$$

As is shown in Fig.18, the first sextant is divided into three time interval. During I interval ($\omega t_0, \omega t_1$) and III ($\omega t_2, \omega t_3$) interval when $\langle v_L \rangle_{T_s} > 0$, i_L is increasing. During II interval ($\omega t_1, \omega t_2$) when $\langle v_L \rangle_{T_s} < 0$, i_L is decreasing. In one sextant, the average voltage across the inductor should be zero.

$$\int_0^{\pi/3} \langle v_L(\omega t) \rangle_{T_s} d(\omega t) = 0 \quad (85)$$

The critical instants ωt_1 and ωt_2 for II interval can be calculated by assuming $\langle v_L(\omega t) \rangle_{T_s} = 0$.

$$\begin{cases} \omega t_1 = -a \cos(\frac{3}{\pi}) + \frac{\pi}{6} \approx 0.2222 \\ \omega t_2 = a \cos(\frac{3}{\pi}) + \frac{\pi}{6} \approx 0.8250 \end{cases} \quad (86)$$

Integrating $\langle v_L(\omega t) \rangle_{T_s}$ in (84) from ωt_1 to ωt_2 , the inductor current ripples can be derived as

$$\Delta I_L \approx -\frac{1}{\omega L} \cdot \int_{0.2222}^{0.8250} \langle v_L(\omega t) \rangle_{T_s} d(\omega t) = \frac{0.0181}{\omega L} \cdot \frac{\sqrt{3}GV_{dc}}{2} = \frac{0.0184\sqrt{3}G}{4\pi} \cdot \frac{V_{dc}}{Lf_{Line}} \quad (87)$$

B. Capacitor requirement

Thus, the charging current of capacitor during non-ST interval i_{C_NST} is as

$$i_{C_NST}(\omega t) = i_L - i_{dc_link}(\omega t) = \begin{cases} i_L - \hat{i}_{ac} \cos(\omega t) & (100) \\ i_L + \hat{i}_{ac} \cos(\omega t + \frac{2\pi}{3}) & (110) \end{cases} \quad (88)$$

From (76) and (88), the average current across the capacitor in one switching time period can be derived and simplified as:

$$\begin{aligned} \langle i_C(\omega t) \rangle_{T_s} &= d_{ST}(\omega t) \cdot (-i_L) + d_{(100)}(\omega t) \cdot (i_L - \hat{i}_{ac}(\omega t)) \\ &+ d_{(110)}(\omega t) \cdot (i_L + \hat{i}_{ac}(\omega t + \frac{2\pi}{3})) \\ &= \frac{3\sqrt{3}\pi G^2 \hat{i}_{ac}}{4(3\sqrt{3}G - \pi)} \left[\cos(\omega t - \frac{\pi}{6}) - \frac{3}{\pi} \right] \end{aligned} \quad (89)$$

v_C increases during II interval, the critical instants ωt_1 and ωt_2 can be calculated by assuming $\langle i_C(\omega t) \rangle_{T_s} = 0$. Obviously, the critical instants ωt_1 and ωt_2 are the same as (86). Similarly, integrating $\langle i_C(\omega t) \rangle_{T_s}$ in (89) from ωt_1 to ωt_2 , the capacitor voltage ripples can be derived as

$$\begin{aligned} \Delta v_C &\approx \frac{1}{\omega C} \cdot \int_{0.2222}^{0.8250} \langle i_C(\omega t) \rangle_{T_s} d(\omega t) \\ &= \frac{0.0181}{2\pi f_{Line} C} \cdot \frac{3\sqrt{3}\pi G^2 \hat{i}_{ac}}{4(3\sqrt{3}G - \pi)} = \frac{0.0181 \cdot 3\sqrt{3}\pi G^2}{8\pi(3\sqrt{3}G - \pi)} \cdot \frac{\hat{i}_{ac}}{f_{line} C} \end{aligned} \quad (90)$$

The capacitor *RMS* current ripples can be calculated as

$$I_{S_rms}^2 = \frac{6}{T_{Line}} \sum d(t) \cdot i_c^2(t) = \frac{3}{\pi} \int_0^{\pi/3} \left[\begin{aligned} & d_{ST}(\omega t) \cdot (-i_L)^2 + d_{(100)}(\omega t) \cdot (i_L - \hat{i}_{ac}(\omega t))^2 \\ & + d_{(110)}(\omega t) \cdot (i_L + \hat{i}_{ac}(\omega t + \frac{2\pi}{3}))^2 \end{aligned} \right] d(\omega t) \quad (91)$$

REFERENCES

- [1] J. Momoh, Renewable Energy and Storage. New York, NY, USA: Wiley, 2012.
- [2] W. Li and X. He, "Review of nonisolated high-step-up DC/DC converters in photovoltaic grid-connected applications," IEEE Trans. Ind. Electron., vol. 58, no. 4, pp. 1239–1250, May 2011.
- [3] F. Z. Peng, "Z-source inverter," IEEE Trans. Ind. Appl., vol. 39, no. 2, pp. 504–510, Mar. 2003.
- [4] Yam P. Siwakoti, Fang Zheng Peng, Frede Blaabjerg, Poh Chiang Loh, and Graham E. Town, "Impedance-Source Networks for Electric Power Conversion Part I: A Topological Review," IEEE Trans. Power Electron., vol. 30, no. 2, pp. 699–716, Feb. 2015.
- [5] Omar Ellabban; Haitham Abu-Rub, "Z-Source Inverter: Topology Improvements Review," IEEE Trans. Ind. Electron Magazine, vol. 10, no. 1, pp. 6–24, Nov. 2016.
- [6] Yu Tang, Shaojun Xie, Chaohua Zhang, and Zegang Xu, "Improved Z-Source Inverter With Reduced Z-Source Capacitor Voltage Stress and Soft-Start Capability," IEEE Trans. Power Electron., vol. 24, no. 2, pp. 833–838, Feb. 2009.
- [7] Wei Qian, Fang Zheng Peng, and Honnyong Cha, "Trans-Z-Source Inverters," IEEE Trans. Power Electron., vol. 26, no. 12, pp. 3453–3463, Dec. 2011.
- [8] F. Gao, P.C. Loh, D. Li, F. Blaabjerg, "Asymmetrical and symmetrical embedded Z-source inverters," IET Trans. Power Electron., vol. 4, no. 2, pp. 181–193, 2011.
- [9] Dong Cao, Shuai Jiang, Xianhao Yu, and Fang Zheng Peng, "Low-Cost Semi-Z-source Inverter for Single-Phase Photovoltaic Systems," IEEE Trans. Power Electron., vol. 26, no. 12, pp. 3514–3523, Dec. 2011.

- [10] Poh Chiang Loh, Ding Li, and Frede Blaabjerg, "T-Z-Source Inverters," *IEEE Trans. Power Electron.*, vol. 28, no. 11, pp. 4880–4884, Nov. 2013.
- [11] Miao Zhu, Kun Yu, and Fang Lin Luo, "Switched Inductor Z-Source Inverter," *IEEE Trans. Power Electron.*, vol. 25, no. 8, pp. 2150–2158, Aug. 2010.
- [12] Minh-Khai Nguyen, Young-Cheol Lim, and Geum-Bae Cho, "Switched-Inductor Quasi-Z-Source Inverter," *IEEE Trans. Power Electron.*, vol. 26, no. 11, pp. 3183–3191, Nov. 2011.
- [13] Hafiz Furqan Ahmed, Honnyong Cha, Su-Han Kim, and Heung-Geun Kim, "Switched-Coupled-Inductor Quasi-Z-Source Inverter," *IEEE Trans. Power Electron.*, vol. 31, no. 2, pp. 1241–1254, Nov. 2016.
- [14] Ding Li, Poh Chiang Loh, Miao Zhu, Feng Gao, and Frede Blaabjerg, "Generalized Multicell Switched-Inductor and Switched-Capacitor Z-Source Inverters," *IEEE Trans. Power Electron.*, vol. 28, no. 2, pp. 837–848, Feb. 2013.
- [15] Yam P. Siwakoti, Fang Zheng Peng, Frede Blaabjerg, Poh Chiang Loh, Graham E. Town, and Shuitao Yang, "Impedance-Source Networks for Electric Power Conversion Part II: Review of Control and Modulation Techniques," *IEEE Trans. Power Electron.*, vol. 30, no. 4, pp. 1887–1906, April. 2015.
- [16] F. Z. Peng, M. Shen, and Z. Qian, "Maximum boost control of the Z-source inverter," *IEEE Trans. Power Electron.*, vol. 20, no. 4, pp. 833–838, Jul. 2005.
- [17] M. Shen, J. Wang, and F. Z. Peng, "Constant boost control of the Z-source inverter to minimize current ripple and voltage stress," *IEEE Trans. Ind. Appl.*, vol. 42, no. 3, pp. 770–778, Jun. 2006.
- [18] Miaosen Shen, Fang Zheng Peng, "Operation Modes and Characteristics of the Z-Source Inverter With Small Inductance or Low Power Factor," *IEEE Trans. Power Electron.*, vol. 55, no. 1, pp. 89–96, Jan. 2008.
- [19] Poh Chiang Loh; D. M. Vilathgamuwa, Y. S. Lai; Geok Tin Chua; Y. Li, "Pulse-width modulation of Z-source inverters," *IEEE Trans. Power Electron.*, vol. 20, no. 4, pp. 1346–1355, July 2005.
- [20] Qin Lei, and Fang Zheng Peng, "Space Vector Pulse width Amplitude Modulation for a Buck-Boost Voltage/Current Source Inverter," *IEEE Trans. Power Electron.*, vol. 29, no. 1, pp. 266–274, Jan. 2014.
- [21] Yu Tang, Shaojun Xie, and Jiudong Ding, "Pulsewidth Modulation of Z-Source Inverters With Minimum Inductor Current Ripple," *IEEE Trans. Power Electron.*, vol. 61, no. 1, pp. 98–106, Jan. 2014.
- [22] Fabricio Bradaschia, Marcelo C. Cavalcanti, Pedro E. P. Ferraz, Francisco A. S. Neves, Euzeli C., "Modulation for Three-Phase Transformerless Z-Source Inverter to Reduce Leakage Currents in Photovoltaic Systems," *IEEE Trans. Ind. Electron.*, vol. 58, no. 12, pp. 5385–5395, Dec 2011.
- [23] Volkan Erginer, Mustafa Hadi Sarul, "A novel reduced leakage current modulation technique for Z-source inverter used in photovoltaic systems," *IET Trans. Power Electron.*, vol. 7, no. 3, pp. 496–502, 2014.
- [24] Nassereddine Sabeur, Saad Mekhilef, Ammar Masaoud "Extended maximum boost control scheme based on single-phase modulator for three-phase Z-source inverter," *IET Trans. Power Electron.*, vol. 9, no. 4, pp. 669–679, 2016.
- [25] Mohamed S. Diab, Ahmed A. Elserougi, Ahmed M. Massoud, Ayman S. Abdel-Khalik, and Shehab Ahmed, "A Pulsewidth Modulation Technique for High-Voltage Gain Operation of Three-Phase Z-Source Inverters," *IEEE Trans. Journal of Emerging and Selected Topics in Power Electronics*, vol. 04, no. 2, June 2016.
- [26] Yushan Liu, Baoming Ge, Haitham Abu-Rub, and Fang Zheng Peng, "Overview of Space Vector Modulations for Three-Phase Z-Source/Quasi-Z-Source Inverters," *IEEE Trans. Power Electron.*, vol. 29, no. 4, pp. 2098–2108, April. 2014.
- [27] P. C. Loh and D. M. Vilathgamuwa, "Transient modeling and analysis of pulse-width modulated Z-source inverter," *IEEE Trans. Power Electron.*, vol. 22, no. 2, pp. 498–507, Mar. 2007.
- [28] M. Shen, Q. Tang, and F. Z. Peng, "Modeling and controller design of the Z-source inverter with inductive load," in *Proc. IEEE Power Electron. Spec. Conf.*, 2007, pp. 1804–1809.
- [29] C. J. Gajanayake, D. M. Vilathgamuwa, and P. C. Loh, "Development of a comprehensive model and a multiloop controller for Z-source inverter DG systems," *IEEE Trans. Ind. Appl.*, vol. 54, no. 4, pp. 2352–2359, Aug. 2007.
- [30] Yuan Li, Shuai Jiang, Jorge G. Cintron-Rivera, Fang Zheng Peng, "Modeling and Control of Quasi-Z-Source Inverter for Distributed Generation Applications," *IEEE Trans. Power Electron.*, vol. 60, no. 4, pp. 1532–1541, April. 2013.
- [31] Yu Tang, Shaojun Xie, "System design of series Z-source inverter with feedforward and space vector pulse-width modulation control strategy," *IET Trans. Power Electron.*, vol. 7, no. 3, pp. 736–744, 2014.
- [32] Kolar JW, Round SD. Analytical calculation of the RMS current stress on the DC-link capacitor of voltage-PWM converter systems. *IEE Proceedings-Electric Power Applications.*, vol. 153, no. 4 pp. 535–43, Jul. 2006.
- [33] M. Shen, J. Wang, and F. Z. Peng, "Comparison of traditional inverters and Z-source inverter for fuel cell vehicles," *IEEE Trans. Power Electron.*, vol. 22, no. 4, pp. 1453–1463, Jul. 2007.
- [34] Jin Li, Jinjun Liu, Zeng Liu. Loss Oriented Evaluation and Comparison of Z-Source Inverters Using Different Pulse Width Modulation Strategies[C]. In proceeding of twenty-fourth Applied Power Electronics Conference and Exposition, 2009: 851–856.
- [35] F. Blaabjerg, J. Pedersen, and A. Elkjaer, "An extended model of power losses in hard-switched IGBT inverters," in *Proc. IEEE Ind. Appl. Conf.*, 1996, pp. 3006–3012.
- [36] A. M. Bazzi, P. T. Krein, and J. W. Kimball, "IGBT and diode loss estimation under hysteresis switching," *IEEE Trans. Power Electron.*, vol. 27, no. 3, pp. 1044–1048, Mar. 2012.
- [37] D. Graovac and M. Pürschel, "IGBT power losses calculation using the data-sheet parameters," *Infineon Tech. Rep.*, Appl. Notes, pp. 3–6, Jul. 2006.



Yan Zhang (S'09-M'14) received the B.S. and M.S. degrees in electrical engineering from Xi'an University of Technology (XAUT), Xi'an, China, in 2006 and 2009 respectively, and the Ph.D. degree in electrical engineering from Xi'an Jiaotong University (XJTU), Xi'an, China, in 2014.

He then joined the XJTU Electrical Engineering School as a teaching faculty from 2014. Since early 2016 he is also a Postdoctoral Research Fellow with the Department of Electrical and Computer Engineering, Queen's University, Kingston, ON, Canada. His research interests include topology, model and control of power electronic systems, high step-up DC-DC converters, and power-electronics applications in renewable energy and distributed generation.



Jinjun Liu (M'97-SM'10) received his B.S. and Ph.D. degrees in Electrical Engineering from Xi'an Jiaotong University (XJTU), China in 1992 and 1997 respectively.

He then joined the XJTU Electrical Engineering School as a faculty. From late 1999 until early 2002, he was with the Center for Power Electronics Systems at Virginia Polytechnic Institute and State University, USA, as a visiting Scholar. In late 2002 he was promoted to a Full Professor and then the head of the Power Electronics and Renewable Energy Center at XJTU, which now comprises 14 faculty members and around 100 graduate students and carries one of the leading power electronics programs in China. He served as an Associate Dean of Electrical Engineering School at XJTU from 2005 to early 2010, and the Dean for Undergraduate Education of XJTU from 2009 to early 2015. He currently holds the position of XJTU Distinguished Professor of Power Electronics, sponsored by Chang Jiang Scholars Program of Chinese Ministry of Education. Dr. Liu coauthored 3 books (including one textbook), published nearly 300 technical papers in peer-reviewed journals and conference proceedings, holds more than 40 invention patents (China/US), and delivered for many times plenary keynote speeches at comprehensive IEEE conferences or China national conferences in power electronics area. He received for 7 times governmental awards at national level or provincial/ministerial level for scientific research achievements or academic/teaching career achievements. He also received the 2006 Delta Scholar Award, the 2014 Chang Jiang Scholar Award, the 2014 Outstanding Sci-Tech Worker of the Nation Award, and the IEEE Transactions on Power Electronics 2016 Prize Paper Award. His research interests are power quality control and utility applications of power electronics, micro-grids for sustainable energy and distributed generation, and more/all electronic power systems.

Dr. Liu has served as the IEEE Power Electronics Society (PELS) Region 10 Liaison and then China Liaison for 10 years, an Associate Editor for the IEEE Transactions on Power Electronics for 10 years, and starting from 2015 the

Vice President for membership of IEEE PELS. He is on Board of China Electro technical Society (CES) and was elected to a Vice President of the CES Power Electronics Society in 2013. He has been the Vice President for International Affairs, China Power Supply Society (CPSS) since 2013 and the inaugural Editor-in-Chief of CPSS Transactions on Power Electronics and Applications since 2016. He has served as a Vice Chair of the Chinese National Steering Committee for College Electric Power Engineering Programs since 2013.



Xinying Li received the B.S degree in electrical engineering from Yang Zhou University, Yang Zhou, China, in 2015. Now he continues pursuing the PHD degree in the school of electrical engineering, Xi'an Jiaotong University (XJTU), Xi'an, China.

His main research contents include topologies and control schemes of new high voltage gain DC-DC converters in renewable energy and modulation strategies of Z source converter.



Xiaolong Ma received the B.S. and M.S. degrees in electrical engineering from Xi'an Jiaotong University (XJTU), Xi'an, China, in 2013 and 2016, respectively. He is currently working as the technical management trainee in General Electric Technology Center, Shanghai, China.

His research interests include modeling and control of power electronic systems, and power electronics applications in renewable energy and distributed generation.



Sizhan Zhou (S'12) received the B.S. degree in electrical engineering from Xi'an Jiaotong University, Shaanxi, China, in 2010, where he is currently working toward the Ph.D. degree at the School of Electrical Engineering, Xi'an Jiaotong University, Xi'an, China.

His current research interests include control of grid-connected converters and renewable/distributed power generation systems.



Hongliang Wang (M'12-SM'15) received the B.Sc. degree in electrical engineering from Anhui University of Science and Technology, Huainan, China in 2004, and received the Ph.D. degree in electrical engineering from Huazhong University of Science and Technology, Wuhan, China in 2011.

From 2004 to 2005, he worked as an electrical engineer of Zhejiang Hengdian Thermal Power Plant. From 2011 to 2013, he worked as a senior system engineer of Sungrow Power Supply Co., Ltd. He is a Post-Doctoral Fellow at Queen's University since 2013.

His research interests in power electronics, include digital control, modulation and multilevel topology of inverter for photovoltaic application and micro-grids application; resonant converters and server power supplies, and LED drivers. He has published more than 50 papers in conferences and journals. He is the inventor/co-inventor of 41 China issued patents, 15 US patents and 6 PCT patents pending.

Dr. Wang is currently a senior member of China Electro-Technical Society (CES); a senior member of China Power Supply Society (CPSS). He serves as a member of CPSS Technical Committee on Standardization; a member of CPSS Technical Committee on Renewable Energy Power Conversion; a vice-chair of Kingston Section, IEEE; a session chair of ECCE 2015; a TPC member of ICEMS2012; a China Expert Group Member of IEC standard TC8/PT 62786.



Yan-Fei Liu (M'94-SM'97-F'13) received his Bachelor and Master degree from the Department of Electrical Engineering from Zhejiang University, China, in 1984 and 1987 and PhD degree from the Department of Electrical and Computer Engineering, Queen's University, Kingston, ON, Canada, in 1994.

He was a Technical Advisor with the Advanced Power System Division, Nortel Networks, in Ottawa, Canada from 1994 to 1999. Since 1999, he has been with Queen's University, where he is currently a Professor with the Department of Electrical and Computer

Engineering. His current research interests include digital control technologies for high efficiency, fast dynamic response dc-dc switching converter and ac-dc converter with power factor correction, resonant converters and server power supplies, and LED drivers. He has authored over 200 technical papers in the IEEE Transactions and conferences, and holds 20 U.S. patents. He is also a Principal Contributor for two IEEE standards. He received Premier's Research Excellence Award in 2000 in Ontario, Canada. He also received the Award of Excellence in Technology in Nortel in 1997.

Dr. Liu serves as an Editor of IEEE Journal of Emerging and Selected Topics of Power Electronics (IEEE JESTPE) since 2013, an associate Editor for IEEE Transactions on Power Electronics since 2001, and a Guest Editor-in-Chief for the special issue of Power Supply on Chip of IEEE Transactions on Power Electronics from 2011 to 2013. He also served as Guest Editor for special issues of JESTPE: Miniaturization of Power Electronics Systems in 2014 and Green Power Supplies in 2016. He serves as Co-General Chair of ECCE 2015 held in Montreal, Canada, in September 2015. He will be the General chair of ECCE 2019 to be held in Baltimore, USA. He has been the chair of PELS Technical Committee on Control and Modeling Core Technologies since 2013 and chair of PELS Technical Committee on Power Conversion Systems and Components from 2009 to 2012.